Journal of Zhejiang University-SCIENCE B (Biomedicine & Biotechnology) in press
www.jzus.zju.edu.cn; www.springer.com/journal/11585
E-mail: jzus_b@zju.edu.cn

Research article

https://doi.org/10.1631/jzus.B2400132

Constructing a PANoptosis-based prognostic signature to evaluate the immune landscape and therapy response in clear cell renal cell carcinoma

Yu DONG[1*], Zitong YANG[1*], Zhinan XIA[1,2*], Jiahao LIAO[1], Zhiming CUI[3], Shenhao XU[1], Bing LIU[1], Liangliang REN[1], Tengda WANG[4], Wei GUO[1], Shuwen WANG[1], Yuyong WANG[5,6]✉, Cheng ZHANG[1]✉

[1]*Department of Urology, the Fourth Affiliated Hospital of School of Medicine, and International School of Medicine, International Institutes of Medicine, Zhejiang University, Yiwu 322000, China*
[2]*Department of Urology, The First Affiliated Hospital, Harbin Medical University, Harbin, Heilongjiang 150081, China*
[3]*Department of Radiology, the Fourth Affiliated Hospital of School of Medicine, and International School of Medicine, International Institutes of Medicine, Zhejiang University, Yiwu 322000, China*
[4]*Department of Urology, Guizhou Provincial People's Hospital, Guiyang 550002, China*
[5]*Department of Urology, Affiliated Hangzhou First People's Hospital, School of Medicine, Westlake University, Hangzhou 310006, China*
[6]*The Fourth School of Medicine Affiliated to Zhejiang Chinese Medical University, Hangzhou 310006, China*

Unedited

Abstract: Objective: To identify PANoptosis-related genes (PRGs) in ccRCC for patient stratification and prognosis prediction. Methods: We used differential expression analysis and weighted gene co-expression network analysis (WGCNA) to identify ccRCC-specific PRGs. A prognostic model, the PANoptosis-index (PANI), was constructed using LASSO and Cox regression. The PANI model, comprising PRGs, was validated through single-cell RNA sequencing (scRNA-seq), immunohistochemistry, and RT-qPCR. Patient cohorts were categorized into high- and low-PANI groups, and the model's performance was appraised using various metrics. External validation was performed with the E-MTAB-1980 dataset. Functional and gene set enrichment analyses distinguished biological differences between groups. Mutational landscapes and tumor immune microenvironments were compared. Sensitivity to immunotherapy and antineoplastic drugs was also predicted using PANI. Proliferation and migration capabilities of *ZBP*1 were assessed by CCK-8 and transwell assays. Results: We identified five PRGs (*ZBP1*, *TNFSF14*, *CDKN3*, *PTHLH*, *and HMOX1*) comprising PANI, independently associated with ccRCC patient prognosis. The PANI-based nomogram, integrated with clinical factors, demonstrated high predictive accuracy for prognosis. High-PANI patients exhibited distinct co-mutation patterns in ccRCC driver genes and lower survival probabilities, with an enriched immune-related functional profile, indicating an activated immune environment. These patients also showed increased sensitivity to immunotherapy and antineoplastic drugs. The knockdown of *ZBP1*, a key PRG in the PANI, significantly reduced ccRCC cell proliferation and migration. Conclusions: PANI provides precise prognosis and immunotherapy response predictions for ccRCC patients, facilitating individualized treatment strategies.

Key words: PANoptosis; ccRCC; Prognosis; Tumor immune microenvironment; Immunotherapy response

✉ Yuyong WANG, b1518118@zju.edu.cn
Cheng ZHANG, zhangcheng13836182568@zju.edu.cn
* The three authors contributed equally to this work
Yu DONG, https://orcid.org/0000-0002-2744-2701
Zitong YANG, https://orcid.org/0000-0003-4716-1090
Zhinan XIA, https://orcid.org/0000-0003-0423-4405
Yuyong WANG, https://orcid.org/0000-0002-7964-4436
Cheng ZHANG, https://orcid.org/0000-0003-3758-5172

Received Mar. 7, 2024; Revision accepted Nov. 29, 2024
Crosschecked xxx. xx, 20xx; Published online xxx. xx, 20xx

© Zhejiang University Press 2025

1 Introduction

Renal cell carcinoma ranks among the 16 most prevalent malignancies in the world. There are more than 430,000 newly diagnosed patients and 180,000 associated deaths annually (Sung et al., 2021). Clear cell renal cell carcinoma (ccRCC), the most frequently diagnosed pathological type, accounts for nearly 75% of all cases. Most ccRCC patients are diagnosed at an early stage, making surgical treatment the primary approach (Santoni et al., 2024). However, 25%-30% of patients present with metastasis at diagnosis, and 30% experience recurrence after surgery, highlighting the need for systemic therapies (Allemani et al., 2018). One of the main strategies for managing advanced ccRCC is targeted therapy. Nevertheless, over time, a substantial number of patients develop resistance to the treatment (Capitanio and Montorsi, 2016). Immunotherapy is an effective option for late-stage ccRCC, as nearly 30% of patients exhibit *PD-L1* overexpression (Rodriguez-Vida et al., 2017). However, not all patients achieve favorable outcomes with immunotherapy (Rini et al., 2019), and some may experience adverse events that limit its effectiveness (Dall'Olio et al., 2021, Guven et al., 2022, Rizzo et al., 2023). Hence, there is a critical need to establish accurate predictive models for ccRCC prognosis and immunotherapy response.

As research on crosstalk among cell death processes in various diseases has progressed (Gurung et al., 2014, Kuriakose et al., 2016, Lamkanfi et al., 2008, Lukens et al., 2014, Malireddi et al., 2010), the concept of "PANoptosis" has emerged (Jiang et al., 2021, Karki et al., 2021, Kuriakose, Man, Malireddi, Karki, Kesavardhana, Place, Neale, Vogel and Kanneganti, 2016, Malireddi et al., 2020, Malireddi et al., 2018, Zheng et al., 2020). PANoptosis represents an inflammatory form of programmed cell death (PCD) that integrates features of necroptosis, apoptosis, pyroptosis, and/or ferroptosis (Lin et al., 2022). Its initiation involves the regulatory interactions of ZBP1, AIM2, and pyrin, culminating in the formation of the AIM2-mediated PANoptosome (Lee et al., 2021), which includes diverse inflammasome sensors and crucial cell death regulators, including caspase-3, -7, and -8 in apoptosis, GSDMD, GSDME, and caspase-1 in pyroptosis, as well as MLKL and RIPK3 in necroptosis (Lee, Karki, Wang, Nguyen, Kalathur and Kanneganti, 2021).

Recent studies have elucidated the role of PANoptosis-related biomarkers in promoting anti-tumor immune responses (Karki et al., 2020, Karki et al., 2021, Park et al., 2021). For instance, RIPK3 activation in colon cancer cells increases cytokine production within the tumor microenvironment (TME), enhancing cytotoxic antitumor immunity (Park, Kim, Park, Hwang, Hong, Park, Kang, Morgan, Cha, Lee, Roe and Kim, 2021). PANoptosis, by triggering systemic inflammation through the release of pro-inflammatory cellular contents, presents a promising strategy for solid tumor immunotherapy (Zhao et al., 2020).

Despite its potential, the role of PANoptosis in ccRCC is not well understood. Our study aimed to assess the prognostic importance of PANoptosis-related genes (PRGs) and to develop a prognostic model, the PANoptosis-index (PANI), for predicting ccRCC prognosis and immunotherapy responsiveness. We conducted a comprehensive evaluation and validation of this model using an external dataset, revealing significant correlations between PANI and the tumor immune microenvironment. Hence, our findings could inform personalized treatment strategies and improve patient prognosis outcomes in ccRCC.

2 Methods

2.1 Data collection and preprocessing

Transcriptional data (HTseq-counts form) of ccRCC and adjacent normal tissues were downloaded from The Cancer Genome Atlas (TCGA) database (2013), with survival and clinical outcomes extracted from the TCGA-KIRC bcrxml file. Transcriptional and clinical profiles of the E-MTAB-1980 project from the Array Express database were used as external validation datasets (Sato et al., 2013). The AnnoProbe package of the R environment was applied for probe ID annotation. Baseline characteristics of the ccRCC patients are summa-

Unedited

rized in Tables 1 and 2. Single-cell RNA sequencing (scRNA-seq) data of 7 ccRCC patients were obtained from the publicly accessible dataset GSE156632 (Zhang et al., 2022). Additionally, we downloaded the IMvigor210 dataset, an external cohort of 348 patients treated with anti-PD-1 therapy, to validate the immunotherapy response (Mariathasan et al., 2018). Immunohistochemical images for ccRCC were sourced from the Human Protein Atlas (HPA) database (Uhlén et al., 2015), while protein expression data were collected from the Clinical Proteomic Tumor Analysis Consortium (CPTAC) database (Ellis et al., 2013).

2.2 Identification of differentially expressed PRGs

A PRG list was generated in accordance with a previously published study (Sun et al., 2023) that extracted the gene list from the GeneCards database using a screening criterion of a relevance score greater than three (Stelzer et al., 2016). Differentially expressed genes (DEGs) between tumor and normal tissues were identified using the DESeq2 package in R (Love et al., 2014), with selection criteria of a $|\log_2\text{FoldChange (log2FC)}| \geq 1$ and a P value <0.05.

2.3 Weighted gene co-expression network analysis (WGCNA)

A co-expression network for PRGs was generated using the R package “WGCNA” (Langfelder and Horvath, 2008). ccRCC samples were clustered through average linkage and Pearson correlation coefficients. The soft-threshold parameter for constructing the co-expression gene network was set at 7. To facilitate module identification, we calculated the topological overlap matrix (TOM) from the adjacency matrix, then computed its dissimilarity measure. Genes exhibiting analogous expression profiles were grouped by constructing a hierarchical clustering tree, with network modules identified using a dynamic tree-cutting algorithm to segment the branches. The module with the highest correlation coefficient and strongest statistical significance was identified as the pivotal module, with its constituent genes selected for downstream analyses.

2.4 scRNA-seq data analysis

The scRNA-seq data analysis was conducted using the "Seurat" package (Stuart et al., 2019). Initially, quality control procedures were applied, retaining genes expressed in at least three cells, with mitochondrial gene content below 10%, and within an expression range of 200 to 7000. Next, 2000 highly variable genes were selected for further investigation. The "Harmony" package was used to address batch effects from different samples. Cell clusters were then identified using the "FindClusters" and "FindNeighbors" functions, with visualization performed via t-distributed stochastic neighbor embedding (t-SNE). Cells were annotated based on marker genes specific to different cell types. Finally, the "AddModuleScore" function within Seurat was used to score each cell on its expression of the specific gene set of interest.

2.5 Model construction by machine learning approaches

Using the "createDataPartition" function in R, ccRCC patients were randomly divided into training and testing cohorts in a 1:1 ratio. We initially identified potential prognostic PRGs via univariate Cox regression analysis, followed by LASSO Cox regression using the "glmnet" package (Friedman et al., 2010) to further refine the selection of key prognostic PRGs. To optimize our model, we conducted a multivariate stepwise Cox regression to identify the most impactful PRGs and constructed a proportional hazards model. Based on this, we developed the PANI equation by integrating the multivariate regression coefficients with the respective PRG expression levels, as follows:

$$\text{PANI}=\sum(\text{Exp}_{\text{gene}} * \text{coef})$$

Additionally, we performed Pearson correlation analysis to identify transcription factors (TFs) and enhancer RNAs (eRNAs) associated with the PRGs in our model, applying a threshold of |Pearson correlation| > 0.4 and P < 0.001. The associations between identified TFs/eRNAs and PRGs were visualized using Sankey diagrams to illustrate potential regulatory relationships.

Unedited

2.6 Survival analysis and nomogram construction

We categorized cohorts, including TCGA, internal training and testing datasets, and E-MTAB-1980, into high- and low-PANI groups using the median PANI value as the threshold. Kaplan-Meier (KM) survival analysis, conducted with the "survminer" R package, was used to assess differences in overall survival (OS) and progression-free survival (PFS) across these groups, with significance evaluated by the log-rank test (P value < 0.05). Using the "timeROC" package, ROC curve analysis was used to measure the sensitivity and specificity of PANI for OS prediction in ccRCC patients, allowing us to compare PANI's AUC with other clinical features.

To further refine our prognostic model and strengthen predictive accuracy, we developed a nomogram that combines the PANI score with individual clinical characteristics, delivering a quantitative survival estimate for ccRCC patients. The nomogram's precision, discriminative ability, and overall effectiveness were assessed using ROC analysis and the C-index, ensuring robust prognostic utility.

2.7 Genomic alteration analysis

Each patient's variants file was retrieved from the TCGA repository. Using the "maftools" R package, we analyzed the mutated genes across different PANI categories and calculated the tumor mutation burden (TMB) for each individual (Mayakonda et al., 2018). This package was also used to generate an oncoplot that visualizes the landscape of genetic variants. Additionally, we used "maftools" to create a heatmap illustrating co-occurring variants, unrelated variants, and mutually exclusive variants, providing deeper insights into the genomic alterations associated with ccRCC in relation to the PANI score.

2.8 Functional enrichment analysis

We began our analysis by calculating the DEGs between the high and low PANI groups, ranking them according to their log2 fold change (log2FC) values. Following this, we used the "org.Hs.eg.db" and "clusterProfiler" R packages to perform functional enrichment analysis, including gene ontology (GO) analysis (Thomas et al., 2022) and gene set enrichment analysis (GSEA) on hallmark gene sets from the MSigDB database (Subramanian et al., 2005). GO enrichment analysis comprised the facets biological process (BP), molecular function (MF), and cellular component (CC) (Thomas, Ebert, Muruganujan, Mushayahama, Albou and Mi, 2022). The statistical significance threshold for GO enrichment analysis was set at a p value < 0.05. We then visualized the top 10 most significantly enriched GO terms across the three categories (CC, BP, and MF), along with the top five most significant terms identified through GSEA.

2.9 Immune-related analysis

We used the "ESTIMATE" R package to evaluate the tumor microenvironment (TME) scores for the PANI groups, including the stromal score, immune score, and estimate score (Yoshihara et al., 2013). To quantify the immune microenvironment, we applied multiple algorithms, including "CIBERSORT," "EPIC," "MCP-counter," "quanTIseq," "TIMER," and "xCell" (Aran et al., 2017, Becht et al., 2016, Chen et al., 2018, Li et al., 2017, Plattner et al., 2020). An immune modulator-related gene list was obtained from the GeneCards database and subsequently filtered by functional relevance score (Stelzer, Rosen, Plaschkes, Zimmerman, Twik, Fishilevich, Stein, Nudel, Lieder, Mazor, Kaplan, Dahary, Warshawsky, Guan-Golan, Kohn, Rappaport, Safran and Lancet, 2016). We conducted a single-sample gene set enrichment analysis (ssGSEA) using the R package "gsva" (Hänzelmann et al., 2013) to assess the enrichment scores of immunocytes and immune function relevant pathways. Spearman correlation analysis was used to examine the relationships between the PANI score, immune cell fractions, and immune functions. Additionally, we performed correlation analysis to assess the relationship between PRG expression levels and immune functions.

2.10 Immunetherapy response prediction

The immunophenoscore (IPS), based on a machine learning algorithm developed from The Cancer Immunome Atlas (TCIA), was calculated for ccRCC patients based on their transcriptional data (Van Allen et al.,

Unedited

2015). This score (including IPS, IPS-CTLA4 blocker, IPS-PD-1/PD-L1/PD-L2 blocker, IPS-CTLA4 and PD-1/PD-L1/PD-L2 blocker) (Van Allen, Miao, Schilling, Shukla, Blank, Zimmer, Sucker, Hillen, Foppen, Goldinger, Utikal, Hassel, Weide, Kaehler, Loquai, Mohr, Gutzmer, Dummer, Gabriel, Wu, Schadendorf and Garraway, 2015) serves as an indicator of their potential response to immunotherapy. IMvigor210, an external dataset comprising 348 patients who received anti-PD-1 treatment, was used to validate immune therapy responses.

2.11 Antineoplastic drug sensitivity prediction

The difference in half maximal inhibitory concentration (IC50) between the groups was assessed by the Wilcoxon signed-rank test. The outcomes were then visually represented as a box plot with the aid of "pRRophetic" and "ggplot2"(Geeleher et al., 2014).

2.12 Cell culture

Human ccRCC cell lines 786-O, A498, and OS-RC-2, as well as the human proximal renal tubular cell line HK-2 as a normal control, were procured from the American Type Culture Collection (ATCC, Manassas, VA, USA). All cell lines were maintained in a culture medium supplemented with 10% fetal bovine serum and 1% penicillin/streptomycin. Cells were incubated at 37 °C in a humidified atmosphere with 5% CO_2. Specifically, RPMI-1640 medium was used for OS-RC-2 and 786-O cells, whereas A498 and HK-2 cells were maintained in minimum essential medium (MEM) with the addition of non-essential amino acids.

2.13 RNA extraction and real-time quantitative PCR (RT-qPCR)

The total RNA of 786-O, A498, OS-RC-2, and HK-2 cells was isolated using the FastPure Cell/Tissue Total RNA Isolation Kit V2 from Vazyme (Nanjing, China). Reverse transcription was subsequently conducted using the HiScript® III 1st Strand cDNA Synthesis Kit (+gDNA wiper) also from Vazyme. RT-qPCR reactions were carried out using Taq Pro Universal SYBR qPCR Master Mix, also from Vazyme. Gene expression levels were assessed using the $2^{-\Delta\Delta Ct}$ method, with GAPDH serving as the endogenous control. These experiments were carried out three times. The primer sequences for *ZBP1*, *CDKN3*, *TNFSF14*, *PTHLH*, and *HMOX1* are provided below:

ZBP1: F: AGAAGAGCAAAGTCAGCCTCAA, R: CCAGCTGTTGGGTCCATTCT;

CDKN3: F: ATCCAATCGCAGATGGAGGG, R: GGAGACAAGCAGCTACAAGACA;

TNFSF14: F: CTCTTGCTGTTGCTGATGGG, R: TCGTGAGACCTTCGCTCTTGT;

PTHLH: F: GTTCGAGGTTCAAAGGTTTGCC, R: AGGTTGGAGGCGAGTTGAAAA;

HMOX1: F: AGTTCAAGCAGCTCTACCGC, R: ACTCCTCAAAGAGCTGGATGT.

2.14 Cell transfection

We purchased 3 siRNAs targeting *ZBP1* from GenePharma (China). Cells were transfected with 20 nM of siRNA using jetPRiME (Polyplus, NY, USA) according to the manufacturer's protocol. The sequences used for siRNA are listed below: si-#1, sense: 5'-CUUCGUUUGAAGCAAGAAUTT-3', antisense: AUUCUUGCUUCAAACGAAGTT; si-#2, sense: 5'-CAAGUCCUCUACCGAAUGATT-3', antisense: 5'-UCAUUCGGUAGAGGACUUGT-3'; si-#3, sense: 5'-GAUGAGCAGUCCAAAGCAUTT-3', antisense: 5'-AUGCUUUGGACUGCUCAUCT-3'. The effectiveness of *ZBP1* knockdown was evaluated through RT-qPCR.

2.15 CCK8 assay

Cell proliferation was assessed using the cell counting kit-8 (CCK-8). Cells from both the experimental and control groups were plated in a 96-well plate at a density of 1000 cells per well. The proliferation of 786O

Unedited

and OSRC2 cells was evaluated using the CCK-8 reagent (Beyotime, Shanghai, China) at 0, 24, 48, and 72 h post-seeding, with a final concentration of 10 μL per well. An automated microplate reader was used to determine the optical density of the reaction mixture at 450 nm.

2.16 Transwell assay

The transwell migration assay was conducted using 24-well transwell chambers (Corning, NY, USA). About 20,000 cells were suspended in serum-free medium and then placed into the upper chamber. In the lower chamber, culture medium containing 10% FBS was added as a chemoattractant. The cells that migrated across the membrane were fixed, stained, and counted under a light microscope, using Image J software for enumeration.

2.17 Wound healing assay

Cells were seeded in 6-well plates and grown to confluence overnight. A scratch was made in the monolayer using a sterile 200-μL pipette tip, and the wells were washed with PBS to remove detached cells. Fresh medium without FBS was added, and incubation was carried out for 24 h in a 5% CO2 atmosphere at 37 °C. Images of the wound area were captured at 0 and 24 h using a phase-contrast microscope. Wound closure was quantified by measuring the area at each time point and calculating the percentage of closure using ImageJ.

2.18 Statistical analysis

Statistical analyses were conducted using R software (version 4.2.3) and GraphPad Prism (Version 9.0.0). Correlation coefficients were assessed using Pearson analysis. Statistical significance was defined as a P value <0.05.

Unedited

3 RESULTS

3.1 Identification of candidate PRGs in ccRCC and construction of PANI

A total of 935 PRGs were compiled (Table S1). Differential expression analysis on these PRGs using TCGA-KIRC transcriptional data identified 274 DEGs. Among them, 64 were downregulated in tumor samples and 210 were upregulated (Figs. 1a and 1b; Table S2). We then applied the WGCNA method to explore co-expression networks in the TCGA-KIRC dataset. A scale-free network was constructed with a soft-thresholding power of β=7 (Figs. S1a and S1b), followed by average linkage hierarchical clustering to identify three distinct gene modules (Fig. 1c). The MEblue module showed the strongest association with tumor samples (r=0.63, P<0.001, Fig. 1d), underscoring its clinical relevance. Within this module, 211 PRGs were confirmed as tumor-related. By overlapping these PRGs with the DEGs, we identified 146 target genes significantly correlated with ccRCC (Fig. 1e).

The TCGA-KIRC patient cohort was randomly divided into a training set (n=267) and a testing set (n=266), maintaining an approximate 1:1 distribution. Using univariate Cox regression analysis, we initially identified 35 PRGs associated with OS in TCGA-KIRC patients (Fig. 1f). To refine these, we applied a LASSO-Cox proportional hazards regression, focusing on highly variable PRGs and integrating clinical data. This approach highlighted 12 PRGs as significant prognostic factors, which were then subjected to a multivariate stepwise Cox regression analysis for further refinement (Figs. 1g and 1h). The final outcome was the development of a prognostic signature, termed PANI, for ccRCC, composed of five key PRGs (Fig. 1i).

We calculated Pearson's correlation coefficients using multivariate Cox regression analysis and derived the PANI using the formula: PANI = (-0.00159290941812923 × *HMOX1* expression) + (0.0316304310931614 × *TNFSF14* expression) + (0.0885646687230549 × *CDKN3* expression) + (0.00169143681747131 × *PTHLH* expression) + (0.152943756716447 × *ZBP1* expression). Using the median PANI as the threshold, all patients were categorized into high- or low-PANI groups.

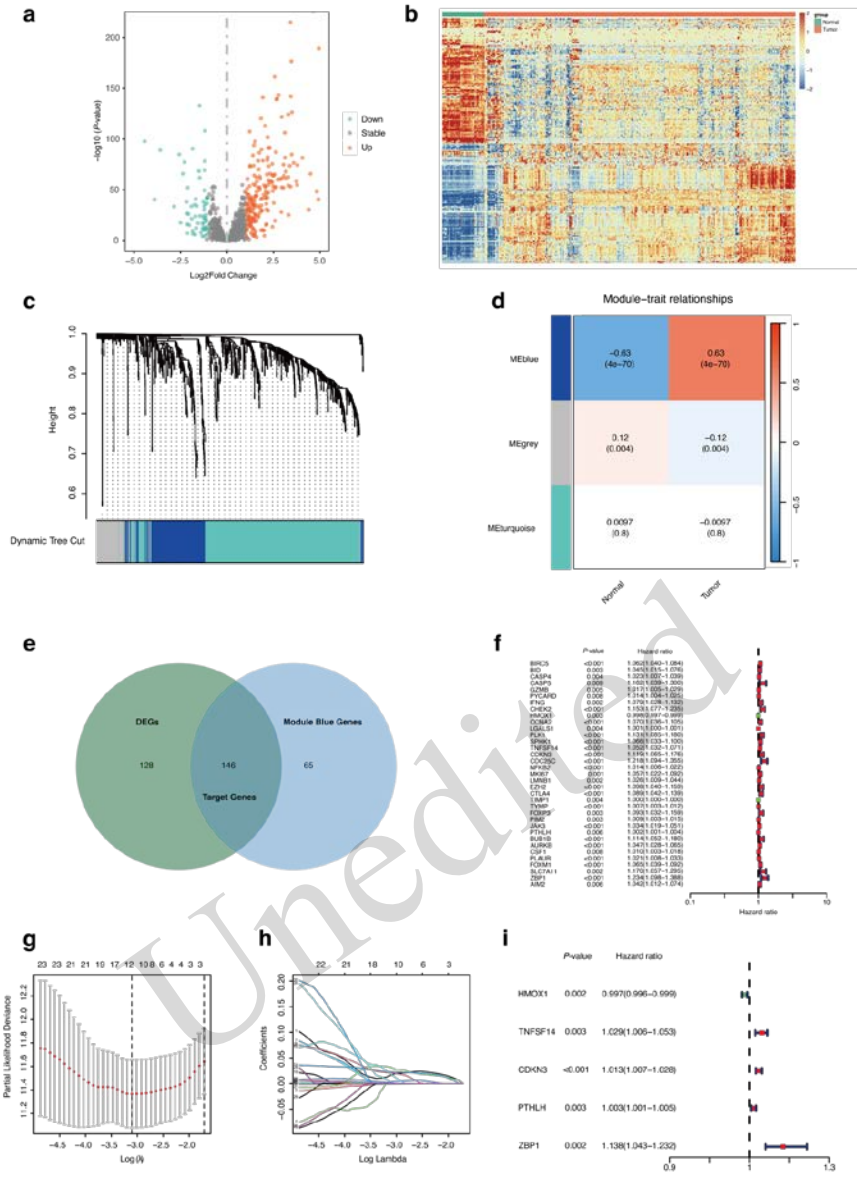

Unedited

Fig. 1 Identification of candidate ccRCC-specific PRGs and construction of the prognostic PANI. (a) Volcano plot of the differentially expressed genes (DEGs) in TCGA, with the threshold set at |logFC| > 1 and a Pvalue < 0.05. Up-regulated DEGs are represented by orange dots, down-regulated DEGs by green dots, and genes that are not significantly differentially expressed by grey dots. (b) Heatmap showing the expression profiles of the DEGs. (c) Tree of gene clusters. The dynamic tree cutting approach was applied to discover modules by separating the tree diagram at significant branch points. This approach was based on an adjacency-based mismatch observed in the hierarchical gene clustering chart. Different colors have been assigned to each module, as indicated in the horizontal bar just below the tree diagram. (d) Associations between modules and traits in normal and malignant tissues. The table is structured so that each row represents a color module, while each column signifies a clinical characteristic. The correlation coefficient between each module and clinical features, along with the corresponding *p* value, is shown in the cells. (e) The Venn diagram is composed of ccRCC-specific DEGs and genes within the blue module associated with ccRCC. The 146 genes that overlap represent the candidate ccRCC-specific PRGs. (f) The forest plot illustrates the prognosis-associated PRGs as identified through univariate Cox proportional hazards regression analysis in ccRCC patients. (g) Penalties were calculated through one thousand rounds of cross-validation to determine the optimal parameter values. (h) LASSO-Cox regression analysis was conducted, using the minimum criterion for parameter selection. (i) The forest plot shows the final set of prognostic PRGs established through multivariate Cox regression analysis in ccRCC patients.

3.2 Validation of expression profiles for prognostic PRGs

To evaluate the expression profiles of these prognostic PRGs, we first analyzed data from the TCGA database. The findings showed that these genes were significantly overexpressed in tumor tissues compared to normal tissues ($P < 0.001$, Fig. 2a). We then measured the expression levels of the five PRGs in normal kidney and ccRCC cell lines using RT-qPCR (Figs. 2b–2f). Results indicated a pronounced increase in mRNA levels of *ZBP1*, *TNFSF14*, *CDKN3*, *PTHLH*, and *HMOX1* in OS-RC-2 and 786-O cells compared to HK-2 cells. In A498 cells, *ZBP1*, *TNFSF14*, and *HMOX1* exhibited a significant rise in expression relative to HK-2 cells, whereas *PTHLH* and *CDKN3* did not show statistically significant increases.

Further examination of their expression profiles in scRNA-seq data revealed that gene set expression scores were markedly elevated in tumor cells compared to endothelial cells (Figs. 2g and 2h). Immunohistochemical analysis provided strong confirmation of *TNFSF14*, *PTHLH*, and *HMOX1* overexpression specific to ccRCC (Figs. S2a-S2c). Additionally, protein expression data reinforced the notable upregulation of *HMOX1* in ccRCC and its strong association with both tumor grade and stage (Figs. S2d). Furthermore, *HMOX1*, identified as a favorable prognostic factor in ccRCC, showed higher expression levels in the low PANI group (Fig. 2i). In contrast, the remaining genes, which are indicative of poorer prognosis in ccRCC patients, were significantly upregulated in the high PANI group.

Additionally, the network of TFs and hub genes, including six TFs and two prognostic PRGs, was illustrated by a Sankey diagram (Fig. 2j). *ZBP1*, the PANoptosome trigger gene, was identified as regulated by three TFs associated with immune regulation, namely *IRF4*, *GFI1*, and *POU2AF1*. Moreover, correlations between eRNAs and hub genes were predicted by Pearson correlation analysis, to explore the underlying regulatory mechanisms in human malignancies. *CDKN3*, recognized as an adverse prognostic marker in ccRCC, showed the highest degree of connectivity and was controlled by five eRNAs (*AC015909.1*, AF196972.1, AL669970.3, GAS1RR, and *TENM3-AS1*) (Fig. 2j).

Unedited

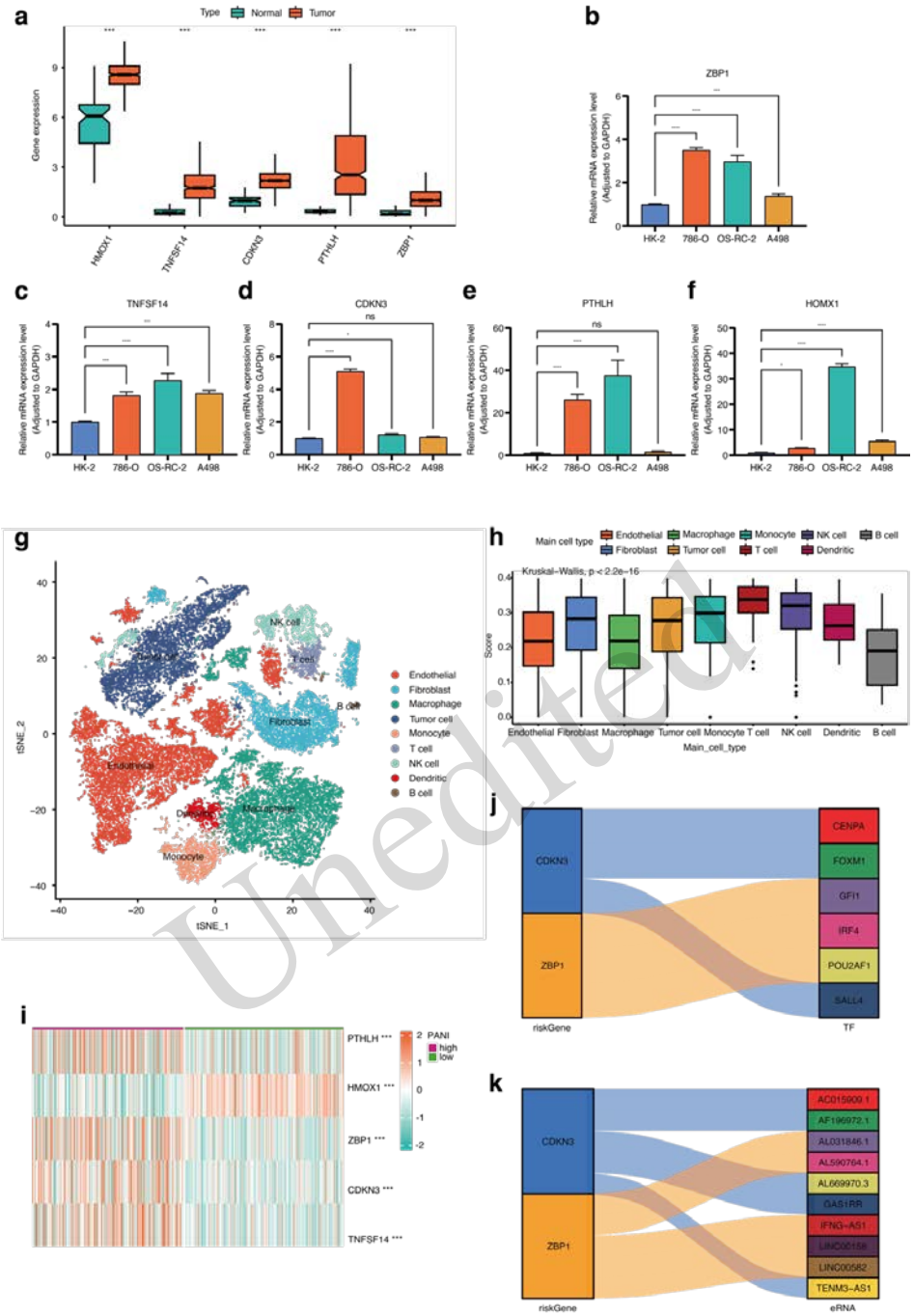

Unedited

Fig. 2 Validation of prognostic PRG expression profiles. (a) The expression profiles of the five PRGs in ccRCC and normal kidney samples were compared using data from the TCGA dataset. Wilcoxon rank-sum tests were used to assess the disparities in gene expression levels between tumor and normal samples. ***P <0.001. (b-f) Relative expression levels of the five PRGs in normal kidney cell lines and ccRCC cell lines were evaluated through RT-qPCR. *P<0.05; ***P<0.001; ****P<0.0001; ns, no statistical significance. (g) A t-SNE visualization shows the scRNA-seq profiles obtained from clinical samples in the GSE156632 dataset. (h) The PANI signature score was computed across various cell types using data from the GSE156632 cohort. (i) A heatmap depicting the expression profiles of the five PRGs in the high-PANI and low-PANI groups sourced from the TCGA dataset. (j) A Sankey diagram illustrating the potential regulatory relationships between PRGs and TFs. (k) A Sankey diagram illustrating the potential regulatory associations between PRGs and eRNAs.

3.3 Validation of the prognostic signature and survival prediction

The prognostic signature developed from the training dataset was rigorously evaluated across multiple independent datasets, including the TCGA dataset, an internal test dataset, and an external validation set (E-MTAB-1980 cohort). Kaplan-Meier (KM) analysis consistently showed that patients with high PANI scores had significantly poorer outcomes across all datasets (TCGA cohort: $P < 0.001$, Fig. 3d; Training cohort: $P < 0.001$, Fig. 3h; Testing cohort: $P = 0.002$, Fig. 3l; E-MTAB-1980 cohort: $P = 0.046$, Fig. 3p). Moreover, in the TCGA cohort, patients in the high PANI group showed a markedly lower PFS rate compared to those in the low PANI group, underscoring the predictive strength of the signature (Fig. 3e).

To further substantiate the predictive accuracy, we conducted receiver operating characteristic (ROC) curve analyses across the datasets. In the TCGA cohort, the area under the curve (AUC) values for OS prediction at 1, 3, and 5 years were 0.729, 0.701, and 0.737, respectively. The corresponding values were 0.715, 0.766, and 0.791 in the training cohort, 0.744, 0.641, and 0.687 in the testing cohort, and 0.811, 0.747, and 0.735 in the E-MTAB-1980 cohort (Figs. 3c, 3i, 3m, and 3q). Collectively, these findings provide robust evidence that PANI is a reliable prognostic biomarker for ccRCC, with strong predictive power across diverse patient cohorts.

Unedited

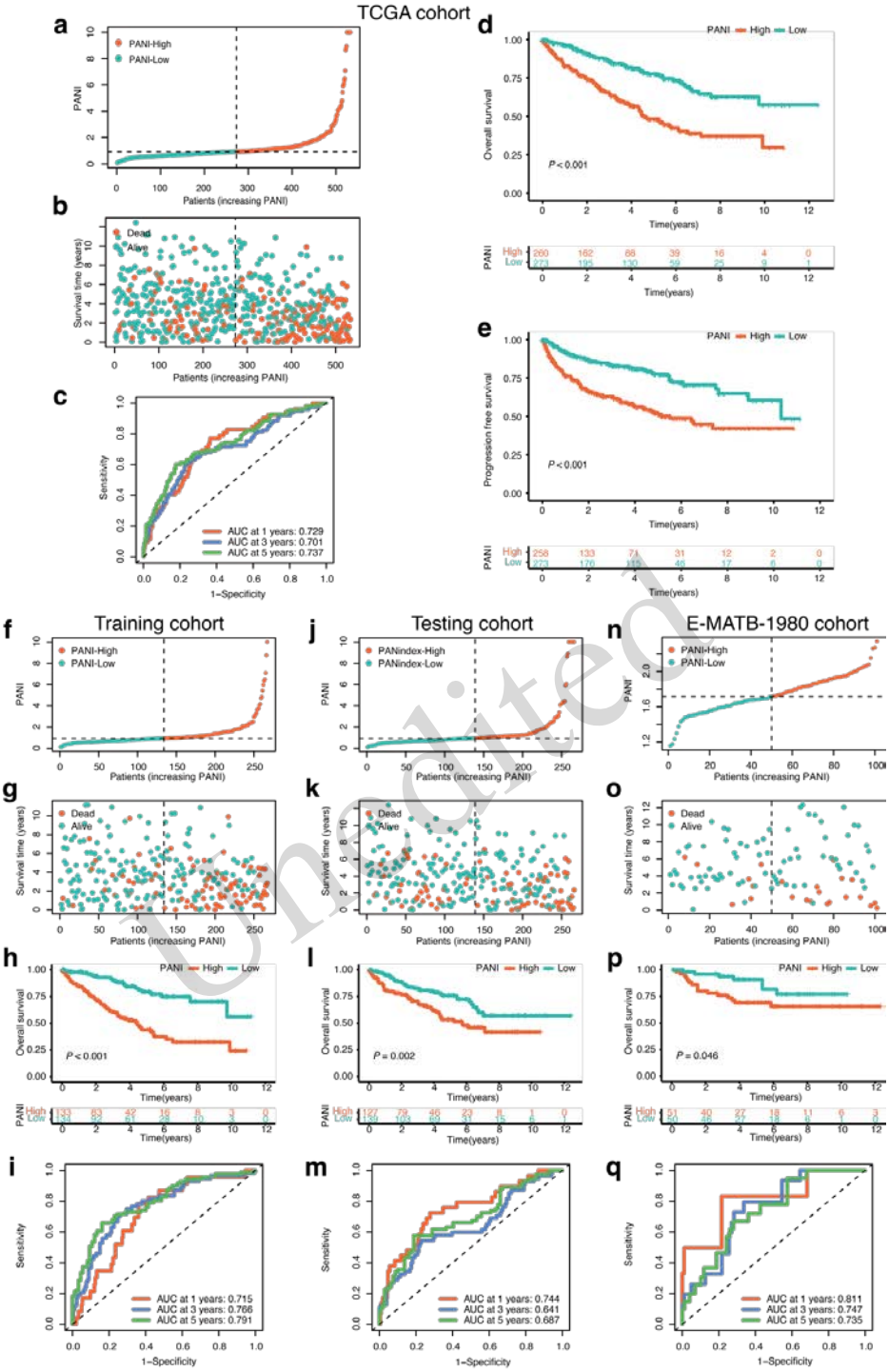

Unedited

Fig. 3 Assessment and confirmation of the predictive performance of the PRG signature in ccRCC. (a, f, j, n) The distribution of PANI in the TCGA group (a), training group (f), testing group (j), and E-MTAB-1980 external validation group (n). (b, g, k, o) Scatter plots illustrating the survival status and PANI scores of ccRCC patients in the TCGA cohort (b), training cohort (g), testing cohort (k), and E-MTAB-1980 cohort (o). (d, h, l, p) Kaplan-Meier curves showing the OS situation per PANI score of the high-PANI group and low-PANI group in the TCGA cohort (d), training cohort (h), testing cohort (l), and E-MTAB-1980 cohort (p). (c, i, m, q) ROC curves showing the predictive performance of PANI with AUC values for 1-year, 3-year, and 5-year OS in ccRCC patients from the TCGA cohort (c), training cohort (i), testing cohort (m), and E-MTAB-1980 cohort (q). (e) Kaplan-Meier curves showing the progression free survival situation per PANI score of the high-PANI group and low-PANI group in the TCGA cohort.

3.4 PANI-based clinical analysis and nomogram construction

The distribution of the PANI and its correlation with patient survival outcomes (Figs. 3a, 3b, 3f, 3g, 3j, 3k, 3n, and 3o) revealed a consistent trend across all four datasets. Higher PANI scores were positively associated with an increase in the proportion of high-risk patients and in the number of deaths. To confirm the clinical relevance of the PANI, we conducted both univariate and multivariate Cox regression analyses, incorporating clinical and pathological variables such as gender, age, clinical stage, and TNM staging. The results strongly indicated that PANI is an independent prognostic factor for ccRCC ($P < 0.001$ and $P = 0.001$, Figs. 4a, 4b).

Further analyses examined the distribution of PANI across various clinicopathological subgroups, including TNM stages and tumor grades. Significant differences in PANI levels were observed when comparing advanced grades and stages (e.g., Grade 4 versus other grades, Stage 4 versus other stages, T4 stage versus other T stages), as well as in patients with distant metastasis (M1) and lymph node involvement (N1), who exhibited notably higher PANI scores than non-metastatic patients (N0 and M0) ($P < 0.05$, Figs. 4c-4g). Finally, a stratified survival analysis was performed to evaluate the PANI's prognostic value within distinct clinicopathological subgroups.

To facilitate clinical application, we constructed a prognostic nomogram that integrates the PANI, tumor grade, and other clinical-pathological factors (Fig. 4i). Gender was excluded due to its negligible impact on outcomes ($P = 0.949$ and $P = 0.908$, Figs. 4a, 4b). ROC curve analysis showed the nomogram's reliable predictive performance, with AUCs of 0.814, 0.794, and 0.754 for 1-year, 3-year, and 5-year OS predictions, respectively (Fig. 4h). Calibration curves confirmed a strong concordance between the predicted and observed OS rates, suggesting high accuracy and clinical utility of the nomogram for patient prognosis in ccRCC (Fig. 4j).

Unedited

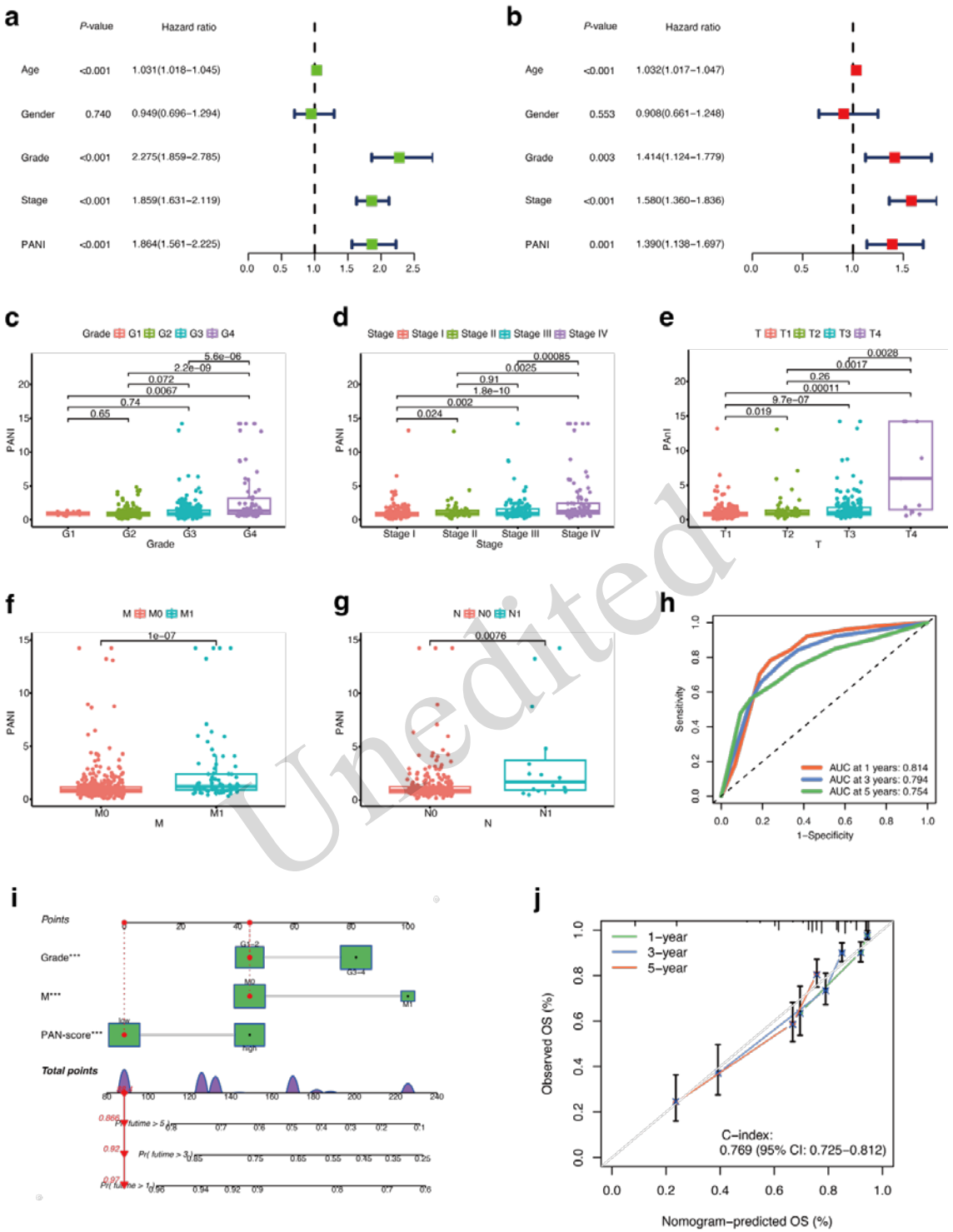

Unedited

Fig. 4 PANI-based clinical analysis and construction of nomogram that incorporates both clinical and pathological variables and the PRG signatures. (a) A Univariate Cox regression examination of OS-related factors. (b) OS-related factors subjected to a multivariate Cox regression analysis. (c-g) Wilcoxon rank-sum tests were used to assess the disparities in association to pathological grade (c), clinical stage (d), tumor infiltration (e), distant metastasis (f), and lymph node involvement (g). (h) The nomogram-based ROC curve analysis shows 1-, 3-, and 5-year OS and the corresponding AUC values for ccRCC patients from the TCGA cohort. (i) The nomogram for prognostic prediction in ccRCC. (j) The calibration curve used to verify the predictive performance of the signature.

3.5 Comparison of genomic alterations between PANI groups

By integrating the mutation data of each patient, we conducted genomic mutation analysis for the PANI groups. In both high- and low- PANI groups, missense mutations were the predominant variant classification (Figs. S3a and S3g). Furthermore, among the variant types, single-nucleotide variants (SNVs) were the most prevalent, with C>T mutations being the primary SNV subtype (Figs. S3b, S3c, S3h, and S3i). Furthermore, to depict differences in the somatic mutation landscape between the two groups, we generated oncoplots that showed the contrasting mutational patterns observed in these two groups. In general, patients with a low PANI were found to have higher mutational frequencies (86.6% *vs* 82.5%, Figs. 5a, b), with the median number of variants per patient in the low PANI group being 46, compared to 43 in the high PANI group (Figs. S3d, S3j). Furthermore, *VHL* and *PBRM1* were the top two mutated genes in the two PANI groups, exhibiting distinct mutation frequencies (53% vs 38% and 43% vs 36%, Figs. 5a, b). Additionally, it was noteworthy that in high PANI group, gene mutations tended to co-occur more frequently than in the low PANI group, where no co-occurrence events were evident (Figs. 5c, d). Notably, in the high PANI group, the ccRCC-triggering gene *VHL* was found to co-occur with *PBRM1* and *SETD2*, which are important co-drivers in ccRCC tumorigenesis (Walton et al., 2023), while being mutually exclusive with *TP53*, a common tumor suppressor gene (Fig. 5c). Given that genomic alterations serve as crucial indicators of genomic instability, we conducted further investigations into the connection between PANI, TMB, and patient prognosis, and it became evident that patients with both high PANI and high TMB had the most unfavorable OS ($P < 0.001$, Fig. S3n).

3.6 Functional enrichment analysis of the PANI groups

To elucidate potential discrepancies in biological functions between different PANI groups, functional enrichment analyses based on the DEGs were introduced. Our analysis unveiled significant enrichments in several immune-related GO terms and pathways within the high-PANI group. These enrichments included terms related to the positive regulation of leukocyte activation, leukocyte-mediated immunity, lymphocyte activation, lymphocyte-mediated immunity, the T cell receptor complex, B cell-mediated immunity, immunoglobulin complex, and activation of the immune response, among others (Fig. 5e). Conversely, catabolism-related GO terms and pathways were notably enriched in the low-PANI group. These encompassed processes like small molecule catabolic processes, organic acid catabolic processes, carboxylic acid catabolic processes, and more (Fig. 5f). Furthermore, the GSEA results highlighted a pronounced association of the high-PANI group with tumor progression. This association was reflected in hallmark pathways, for instance, E2F targets, epithelial mesenchymal transition, and the G2M checkpoint (Fig. 5g). In contrast, the low-PANI group was related to the reactive oxygen species pathway (Fig. 5h).

Unedited

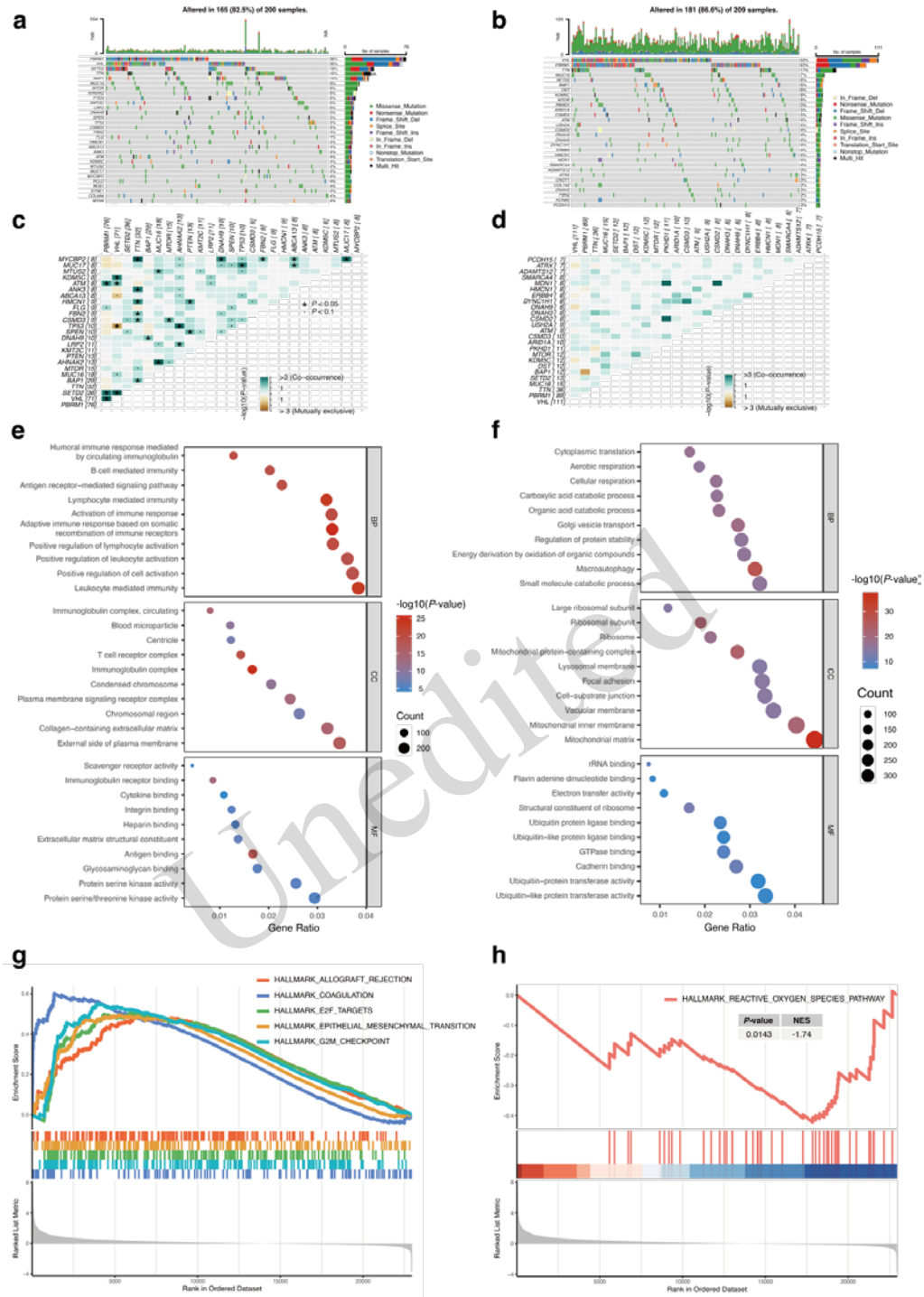

Unedited

Fig. 5 Comparison of genomic alterations and functional enrichment analysis between the two PANI groups. (a) The 30 most frequently mutated genes in the high-PANI group. (b) The 30 most frequently mutated genes in the low-PANI group. (c) Heatmap illustrating the co-mutated states of the commonly mutated genes in the high-PANI group. (d) Heatmap illustrating the co-mutated states of the commonly mutated genes in the low-PANI group. (e) Functional enrichment analysis of upregulated genes in the high-PANI group based on gene ontology. (f) Functional enrichment analysis of up-regulated genes in the low-PANI group based on gene ontology. (g) GSEA based on hallmark gene sets, revealing the pathways enriched in the high-PANI group. (h) GSEA based on hallmark gene sets, revealing the pathways enriched in the low-PANI group.

3.7 Comparison of TME between the PANI groups

The results from GO functional enrichment analysis demonstrated a pronounced enrichment of immune pathways in the high-PANI group. To delve deeper into this observation, the ESTIMATE algorithm was used to evaluate the stromal scores, ESTIMATE scores, immune scores, and tumor purity of the ccRCC patients. The outcomes indicated a substantial difference, with high-PANI group showing significantly higher immune scores ($P < 0.001$) and ESTIMATE scores ($P < 0.01$), compared with the low-PANI group. Furthermore, tumor purity was notably lower in high-PANI group ($P < 0.01$, Fig. 6b). These findings collectively suggested a substantial activation of the immune state in high-PANI group. Notably, a high immune score indicated a poorer outcome in ccRCC (Fig. S4).

Next, we used a variety of algorithms to comprehensively evaluate the tumor immune microenvironment. We noticed a markedly elevated infiltration of immunocytes in the high-PANI group (Fig. 6a). This was reflected in a greater abundance of plasma cells, CD8+ T cells, CD4+ memory activated T cells, T cells follicular helper, T regulatory cells (Tregs), and M1 macrophages (Fig. 6c). A barplot was used to provide the immune cell landscapes across all ccRCC patients (Fig. 6e). Furthermore, we assessed the expression of various immunomodulators between the low and high-PANI groups, including adhesion molecules, antigen presentation factors, co-stimulatory molecules, ligands, and other immunomodulatory markers. These molecules were upregulated in the high-PANI group (Fig. 6d). For further validation, ssGSEA was applied to evaluate the enrichment scores for immunocytes and the activity of immune-related pathways. These results provided additional confirmation of our previous discoveries, indicating that the high-PANI group not only exhibited increased immune cell infiltration but also heightened immune activation (Fig. 6f).

Furthermore, we created a butterfly plot to explore the relations between PANI levels and the infiltration of immunocytes as well as immune functions. Apart from APC co-stimulation and HLA function, eleven other immune-related pathways exhibited significant correlations with PANI (Fig. 6g). Meanwhile, except for NK cells, macrophages and T cells follicular helper, most immunocytes showed significant correlations with PANI (Fig. 6g). This outcome further validated the increased immunological activity within the high-PANI group. Additionally, we explored the correlations between prognostic PRGs and immunocyte infiltration, revealing that *ZBP1*, *CDKN3* as well as *TNFSF14* were positively related to the immune microenvironment (Fig. 6h).

Unedited

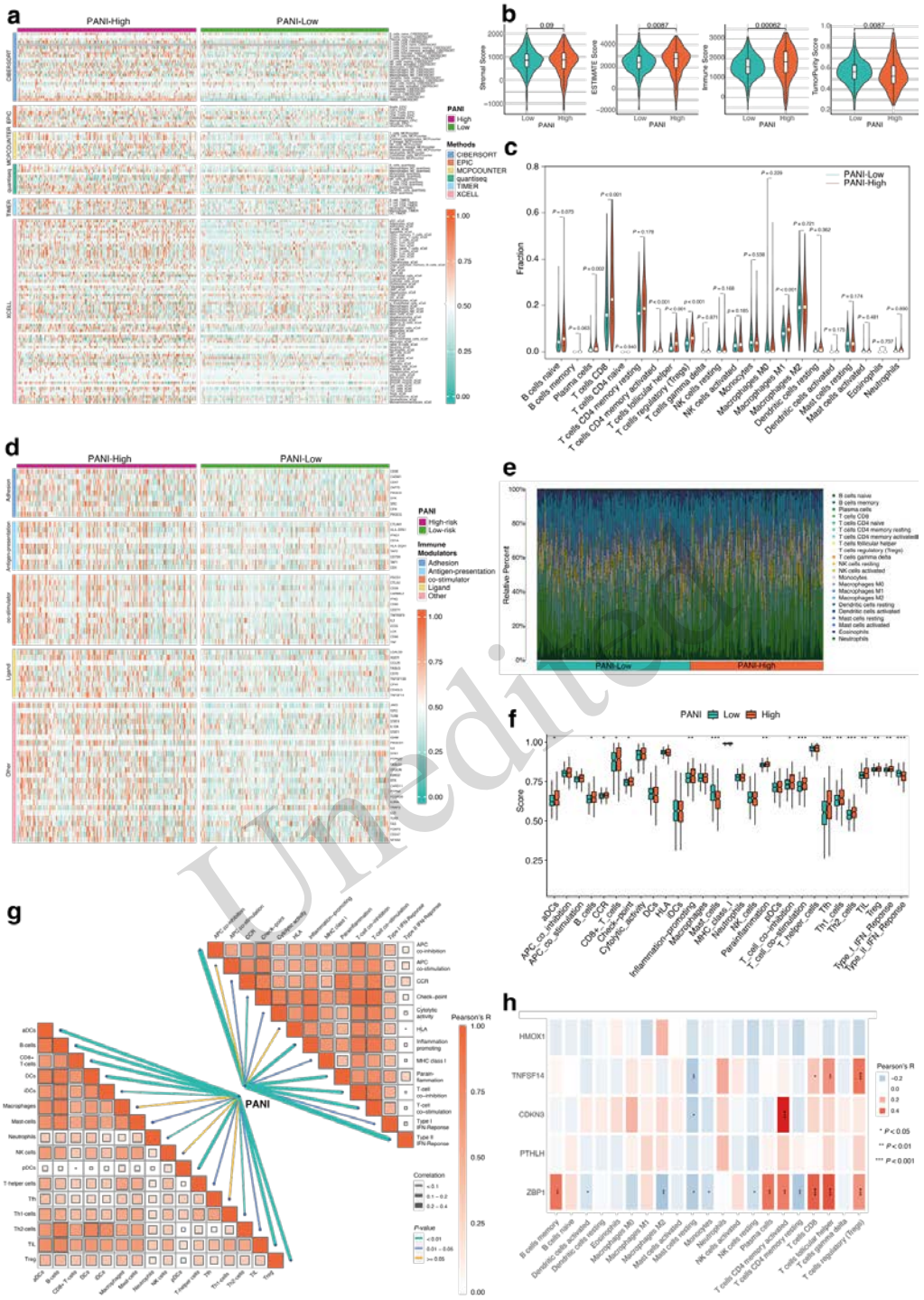

Fig. 6 Comparative analysis of the tumor microenvironment between PANI groups (a) Heatmap illustrating the landscape of immune cell infiltration in the two groups. (b) Comparison of ESTIMATE score, immune score, stromal score, and tumor purity in the low-PANI and high-PANI groups. (c) Analysis of the fraction of infiltrating immune cells between the two groups. (d) Heatmap showcasing the landscape of immune-related functions in the two PANI groups. (e) Boxplot showing the relative percentage of immune cells in each ccRCC patient. (f) ssGSEA analysis of the disparities in immune infiltration levels and immune-related functions between the low- and high-PANI groups. (g) Butterfly plot illustrating the association between PANI and the fraction of immune cells and immune-related functions. (h) Heatmap depicting the association between the five PRGs and immune cells.

Unedited

3.8 Comparison of immunotherapy response between the PANI groups

Immune checkpoint inhibitors (ICIs) represent a promising category of cancer therapy drugs designed to enhance patients' immune function for combating tumor cell proliferation (Dutta et al., 2023). Considering the reported correlation between immune checkpoint gene (ICG) expression and the clinical effectiveness of ICIs, a comparative analysis of ICGs was performed in high-PANI and low-PANI groups. Our results unveiled substantial disparities in the expression of various ICGs between these PANI groups, highlighting distinct immunological profiles and effects of immunotherapy (Fig. 7a). Then we looked into the relationship between two pivotal immune checkpoint genes, *PDCD1* and *CTLA4*, and PANI levels. This analysis revealed a significant association, showing that elevated PANI was closely linked to increased expression of these key immune checkpoints (Figs. 7b, 7c). This discovery further reinforced our conclusion that there are potential differences in the response to ICIs between the two PANI groups. Furthermore, the IPS difference analysis indicated that higher PANI patients, who were treated with either CTLA4 blocker monotherapy (P=0.045) or a combination therapy involving CTLA4 as well as PD-1/PD-L1/PD-L2 (P=0.011), might experience a more favorable outcome compared to individuals with lower PANI (Figs. 7e, 7g). As we lacked access to data from ccRCC patients treated with immunotherapy, we obtained the IMvigor210 dataset, an external cohort comprising 348 patients who received anti-PD-1 therapy. This dataset was used to validate our prognostic PANI signature and offer indirect evidence for the prediction of immunotherapy efficacy in ccRCC patients. Analysis indicated that patients who achieved complete response (CR) or partial response (PR) exhibited elevated PANI levels (Fig. 7h). Conversely, a greater proportion of patients in the low-PANI groups manifested either progressive disease (PD) or stable disease (SD) (Fig. 7i). These findings imply that individuals with heightened PANI levels had a higher possibility of benefiting from ICI therapy.

3.9 Antineoplastic drug sensitivity prediction

Sensitivity of antineoplastic drugs in the ccRCC population across various PANI groups was assessed by analyzing IC50 values. The high-PANI groups had lower IC50 values, indicating increased sensitivity to several drugs, including the mTOR inhibitor AZD2014, the pan-AKT pathway inhibitor AZD5363, as well as poly ADP ribose polymerase (PARP) inhibitors like talazoparib and Olaparib (Figs. 7j-7n).

Unedited

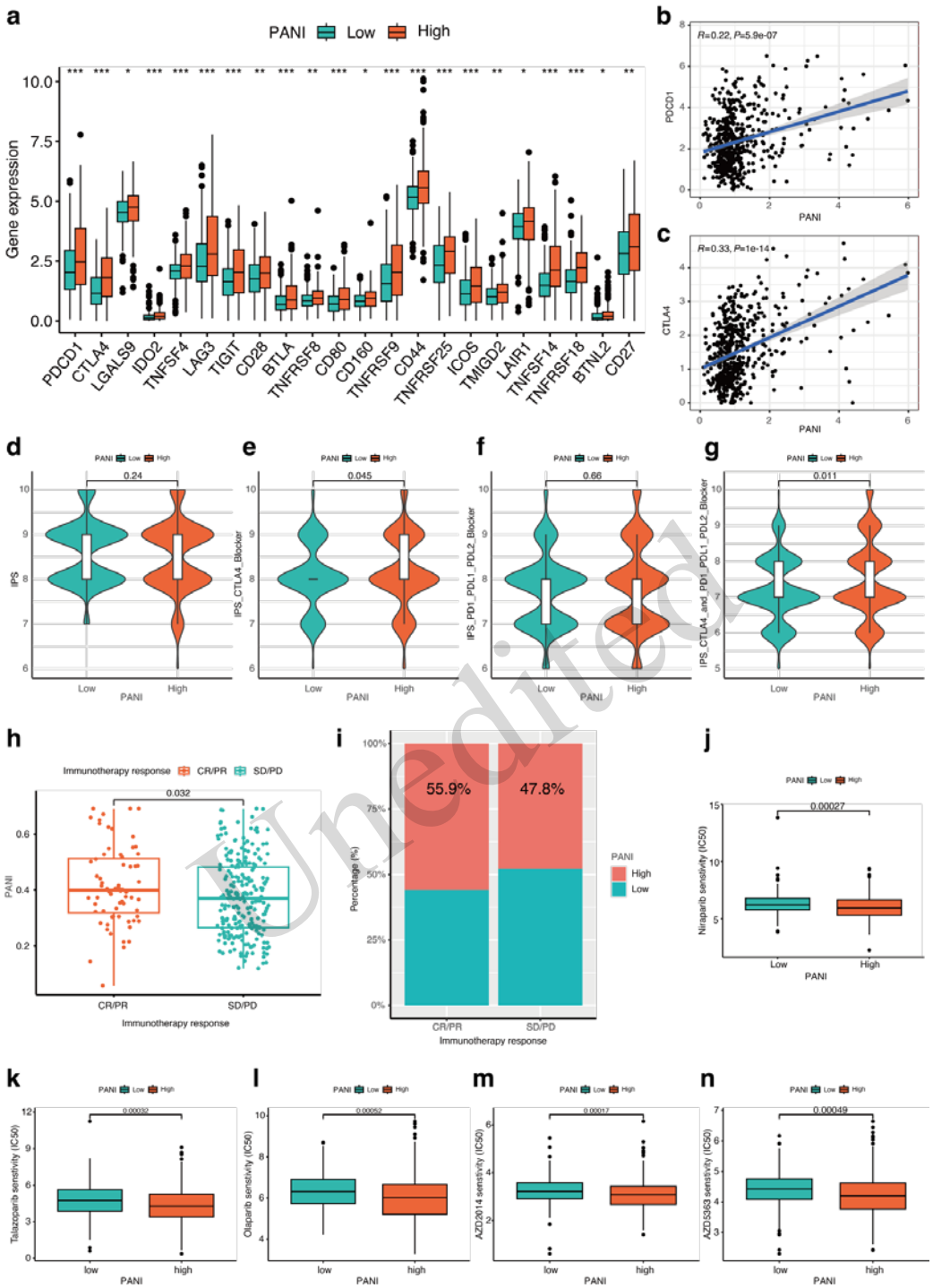

Fig. 7 Comparison of immunotherapy response and antineoplastic drugs sensitivity between PANI groups. (a) Boxplot illustrating the disparity in expression levels of immune checkpoint genes between the low-PANI and high-PANI groups. ****P*<0.05; *****P***<0.01; ******P***<0.001. (b) Pearson correlation analysis revealing the association between PANI and PDCD1 expression. (c) Pearson correlation analysis revealing the association between PANI and CTLA4 expression. (d–g) Violin plot depicting the disparities in response to ICIs between the low- and high-PANI groups. (h) Boxplot showing the distribution of PANI scores among ccRCC patients with different immunotherapy responses. (i) Bar graph showing the percentage of responses to immunotherapy in the low and high PANI groups. (j-n) IC50 values of antineoplastic drugs compared between the low and high PANI groups.**

Unedited

3.10 Identification of the carcinogenic effect of ZBP1 on ccRCC

In our PANI, *ZBP1* exhibits a higher risk coefficient and is significantly overexpressed at the transcriptomic level in ccRCC patients (Fig. 2a), suggesting its potential carcinogenic effect. Consequently, we delved into the *ZBP1* gene. First, we confirmed the overexpression of *ZBP1* in ccRCC cell lines (Fig. 2b). Subsequently, we conducted RNA interference on 786O and OSRC2 cells, followed by verification of the efficiency of *ZBP1* knockdown through RT-qPCR (Figs. 8a, 8b). Knockdown of *ZBP1* markedly suppressed the proliferation activity of ccRCC cells (Figs. 8c, 8d). Furthermore, transwell and wound healing assays revealed a significant decrease in ccRCC cell migration post-ZBP1 knockdown (Figs. 8e, 8f, and 8h), suggesting that *ZBP1* contributes to the progression of ccRCC.

Unedited

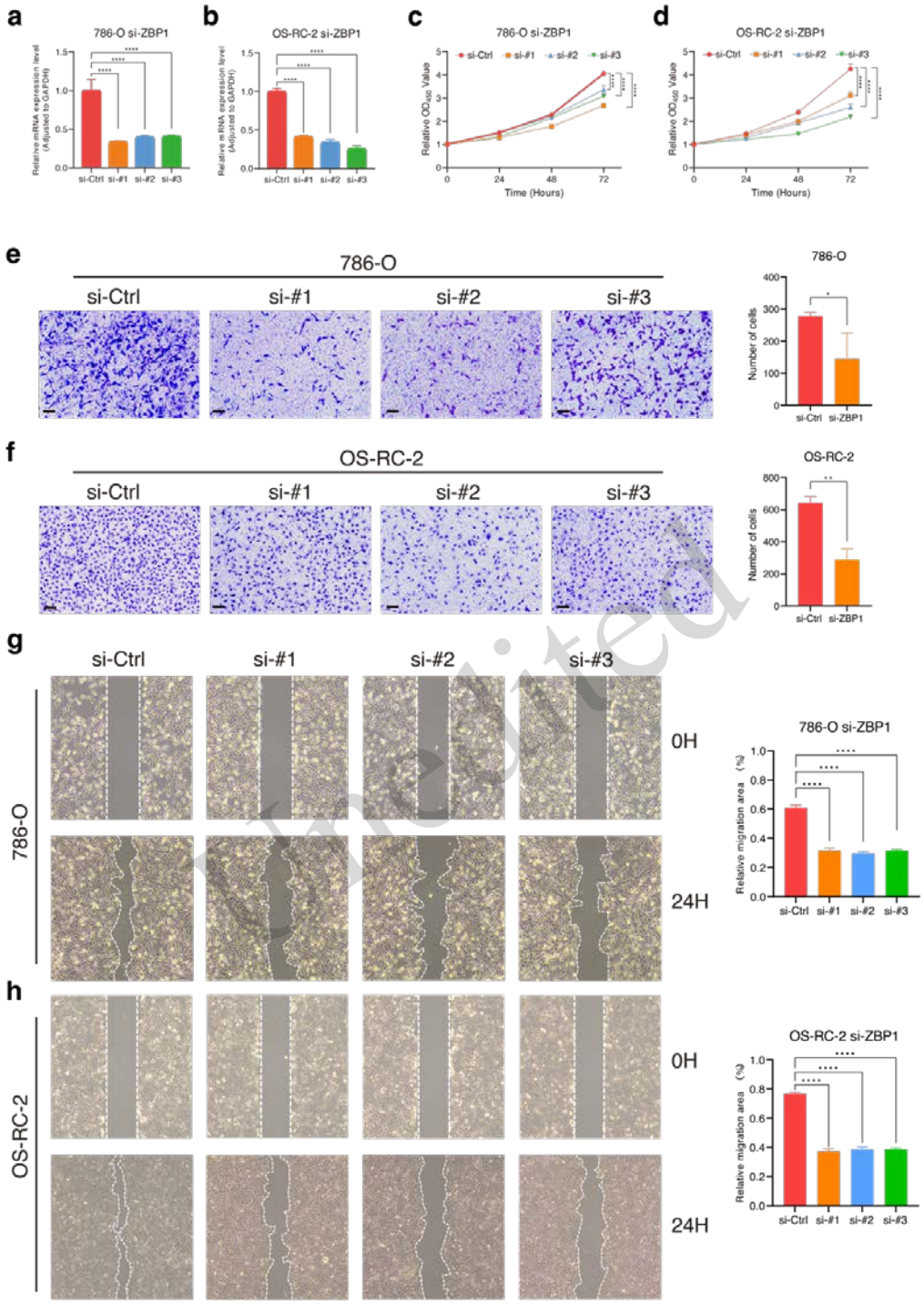

Fig. 8 ***ZBP1*** **knockdown inhibits ccRCC cell proliferation and migration. (a, b) The knockdown efficiency of different siRNA-*ZBP1* constructs in 786O and OSRC2 cells was evaluated using RT-qPCR. ****P*<0.05; *****P*<0.01; ******P*<0.001; *******P*<0.0001. (c, d) The effect of transfection with siRNA–#1, siRNA–#2, siRNA–#3, or negative control (si-Ctrl) on cell proliferation was evaluated using CCK-8 assays. (e-h) The effect of transfection with siRNA–#1, siRNA–#2, siRNA–#3, or negative control (si-Ctrl) on cell migration ability was evaluated using transwell assays (e, f), and wound healing assays (g, h).**

4 Discussion

Neoplasms remain the main killer worldwide(Hu et al., 2016, Zhang et al., 2023). ccRCC is an intricate and heterogeneous malignancy, rendering the prediction of patient prognosis challenging. Advances in high-throughput sequencing and bioinformatics have furnished indispensable tools for investigating prognostic biomarkers, clinical stratification, and disease recurrence detection (Kyrochristos et al., 2019, Wang et al., 2009). Hence, it is of great importance to uncover clinical applicable prognostic biomarkers in ccRCC, with the aim of refining prognostic evaluations of disease progression, estimating overall survival, and customizing treatment strategies.

The expanding understanding of PCD mechanisms has revealed distinct molecular characteristics inherent to various PCD pathways, leading to the concept of PANoptosis. PANoptosis is an intricately coordinated system characterized by complex interactions among multiple cell death pathways that regulate tumorigenesis (Ketelut-Carneiro and Fitzgerald, 2022). Unlike a single death pathway, PANoptosis functions through synergistic interactions within the same cell, either concurrently or sequentially (Chen et al., 2023, Karki, Sharma, Lee, Banoth, Malireddi, Samir, Tuladhar, Mummareddy, Burton, Vogel and Kanneganti, 2020). Moreover, various PCD pathways can complement one another, being triggered either simultaneously or sequentially in response to signals from the tumor microenvironment (Ketelut-Carneiro and Fitzgerald, 2022). For example, if apoptosis is inhibited in cancer cells undergoing immunotherapy, other PCD pathways like pyroptosis, necroptosis, or ferroptosis can be activated to eliminate cancer cells. The integration of these PCD pathways can significantly impact the immune microenvironment and tumor resistance. PANoptosis in cancer cells can trigger strong anti-cancer immune responses, and immunotherapy can work synergistically, even in cases of immune checkpoint inhibitor (ICI) resistance (Tang et al., 2020).

To predict the prognosis and immunotherapy effectiveness in ccRCC, we performed differential expression and WGCNA analysis on bulk transcriptomic data from renal cancer and normal kidney tissues, identifying 146 PRGs significantly associated with ccRCC. Using an integrated machine learning approach, we pinpointed five PRGs (*ZBP1, TNFSF14, CDKN3, PTHLH, and HMOX1*) that form the PANI for prognosis prediction. We validated the cancer-specific high expression of these PRGs through scRNA-seq data from clinical samples, immunohistochemistry from the Human Protein Atlas, and RT-qPCR in renal cancer cell lines. These results highlight the clinical potential of our PANI signature. Notably, *ZBP1*, an interferon-inducible protein and inflammasome sensor, has been recognized as a key instigator of PANoptosis, capable of activating the NLRP3 inflammasome and PANoptosome (Kuriakose, Man, Malireddi, Karki, Kesavardhana, Place, Neale, Vogel and Kanneganti, 2016, Lee, Karki, Wang, Nguyen, Kalathur and Kanneganti, 2021). *ZBP1* plays a pivotal role in PANoptosis, and its deletion alone is sufficient to inhibit PANoptosis (Kuriakose, Man, Malireddi, Karki, Kesavardhana, Place, Neale, Vogel and Kanneganti, 2016). *TNFSF14*, a member of the TNF family, is recognized for promoting T cell proliferation, supporting dendritic cell growth, and inducing apoptosis in cancer cells (Nallar et al., 2017). It has been shown to reverse immunosuppressive microenvironments and enhance anti-tumor immune responses (Ramachandran et al., 2023, Zhang et al., 2023). *CDKN3* was verified to be able to promote cancer cell proliferation and is linked to tumor cell apoptosis (Li et al., 2022, Ma et al., 2023, Yu et al., 2017). While the role of *PTHLH* in PANoptosis remains underexplored, *HMOX1*, a key regulator of ferroptosis, plays a dual role of protection and cytotoxicity (Adedoyin et al., 2018, Chen et al., 2021, Tang et al., 2021). Normally, *HMOX1* exerts a protective role against PCD but excessive *HMOX1* activity can induce cellular ferroptosis, referred to as atypical ferroptosis (Hassannia et al., 2018). To better understand the regulatory mechanisms behind the heightened expression of PRGs in ccRCC, we predicted the potential transcription factors and enhancer RNAs involved in their regulation.

We successfully predicted PFS and OS outcomes for patients across the training, testing, and entire datasets using the PANI. External dataset validation further confirmed its reliability. Univariate and multivariate Cox regression analyses established PANI as an independent prognostic factor in ccRCC. Stratified analyses,

Unedited

incorporating various clinical variables such as age, pathological stage, and grade, affirmed the broad clinical applicability of the model. Additionally, a diagnostic nomogram was developed and validated, incorporating PANI and key clinical features. The strong correlation between predicted and actual 1-year, 3-year, and 5-year OS in ccRCC patients underscores its potential as a clinically relevant prognostic tool.

PANoptosis is characterized by distinct features, such as plasma membrane rupture and the release of cellular contents, which trigger inflammatory responses through complex interactions among various cell death pathways (Ketelut-Carneiro and Fitzgerald, 2022). Our pathway enrichment analysis for the high PANI group revealed significant enrichment in immune-related pathways. Additionally, a detailed analysis of the tumor microenvironment in the high PANI group showed notable alterations, including increased immune scores, elevated ESTIMATE scores, and reduced tumor purity scores. Multiple algorithmic evaluations consistently highlighted increased immune cell infiltration and prolonged activation of immune functions, indicating a robust state of immune activation in the high PANI group.

Furthermore, the high PANI group also showed a significant upregulation of immune checkpoint genes (ICGs), a higher IPS score for CTLA4 blockade, and increased responsiveness to CTLA4 and PD-1/PD-L1/PD-L2 blockade therapies, along with a greater rate of CR or PR to immunotherapy. These findings strongly suggest that patients in the high PANI group may experience enhanced effectiveness of ICIs. Overall, our PANI signature shows promise as a clinically valuable tool for predicting immune status and the responsiveness of ccRCC patients to immunotherapy. Additionally, the co-mutation of key driver genes of ccRCC, such as VHL, PBRM1, and SETD2, in the high PANI group further emphasizes the association between PANI and tumor progression. GSEA revealed a significant enrichment of pathways related to tumor evolution in this group. This suggests that the accelerated tumor progression observed in the high PANI group may contribute to its unfavorable prognosis, providing further insights into the molecular underpinnings of ccRCC progression.

Unedited

We have successfully developed a prognostic index based on five PRGs, offering novel insights and potential biomarkers for predicting prognosis and immunotherapy effectiveness in ccRCC. However, there are some limitations to consider. First, the study relied solely on data from the TCGA public database for model construction, highlighting the need for validation using larger and more diverse clinical datasets. Additionally, bulk RNA-seq data analysis may overlook intercellular differences and the complex interactions within the TME. To further validate the model, more open-access data on kidney cancer immunotherapy are needed. Lastly, further research is essential to explore and uncover the underlying mechanisms of PANoptosis in ccRCC and its potential therapeutic implications.

5 Conclusions

We have successfully developed PANI, a robust prognostic index that holds promise for enhancing prognosis prediction and guiding personalized treatment strategies in ccRCC. This signature, composed of five key PRGs (*ZBP1*, *TNFSF14*, *CDKN3*, *PTHLH*, and *HMOX1*), not only accurately predicts PFS and OS in ccRCC patients but also demonstrates its clinical applicability through validation in external datasets. Furthermore, PANI serves as an independent prognostic factor, even after stratifying for various clinical factors. Our investigation revealed a strong correlation between PANI and immune-related pathways, indicating heightened immune activation marked by increased immunocyte infiltration and elevated immune functions within the high-PANI group. This group also exhibited increased ICGs expression and a favorable response to ICIs, which bodes well for the potential efficacy of immunotherapy. Additionally, the co-mutated status of driver genes and pathway enrichment findings offer insights into the unfavorable prognosis observed in the high PANI group. Moreover, we verified the carcinogenic effect of *ZBP1*, the most significant component of PANI, through in vitro experiments.

Data availability statement

The data presented in this study are publicly available in the NCBI Gene Expression Omnibus (GEO) repository (GSE156632), The Cancer Genome Atlas (TCGA-KIRC, https://portal.gdc.cancer.gov/) database, the Array Express database (E-MTAB-1980, https://www.ebi.ac.uk/arrayexpress), and a freely available, fully documented data package under the Creative Commons 3.0 license that can be downloaded from http://research-pub.gene.com/IMvigor210CoreBiologies. The datasets used or analyzed during the current study are available from the corresponding author upon reasonable request.

Acknowledgments

The authors extend their gratitude to all researchers who contributed to the public dataset employed in the study. The corresponding author had full access to the data used in this research and assumes responsibility for the data's integrity and accuracy. This work was funded by the Natural Science Foundation of Zhejiang Province (grant number LZ22H160008); the Zhejiang Medical Science and Technology Project (grant number 2022RC059); and the Zhejiang Medical Science and Technology Project (grant number 2023KY931).

Author contributions

Yuyong WANG and Cheng ZHANG conceived and supervised the study; Zitong YANG, Yu DONG, Zhinan XIA, Jiahao LIAO, Zhiming CUI, and Shenhao XU designed and performed experiments; Yu DONG, Zitong YANG, Bing LIU, Liangliang REN, Tengda WANG, and Wei GUO analysed data; Shuwen WANG participated manuscript revision; Yu DONG, Zitong YANG, and Zhinan XIA wrote the manuscript. All authors read and approved the final manuscript.

Compliance with ethics guidelines

Yu DONG, Zitong YANG, Zhinan XIA, Jiahao LIAO, Zhiming CUI, Shenhao XU, Bing LIU, Liangliang REN, Tengda WANG, Wei GUO, Shuwen WANG, Yuyong WANG, and Cheng ZHANG declare that they have no conflict of interest.

This work does not contain any studies with human or animal subjects performed by any of the authors.

Unedited

References

Adedoyin, O., Boddu, R., Traylor, A., Lever, J.M., Bolisetty, S., George, J.F., et al., 2018. Heme oxygenase-1 mitigates ferroptosis in renal proximal tubule cells, **314**(5):F702-F714. [doi: 10.1152/ajprenal.00044.2017]

Allemani, C., Matsuda, T., Di Carlo, V., Harewood, R., Matz, M., Nikšić, M., et al., 2018. Global surveillance of trends in cancer survival 2000-14 (CONCORD-3): analysis of individual records for 37 513 025 patients diagnosed with one of 18 cancers from 322 population-based registries in 71 countries, **391**(10125):1023-1075. [doi: 10.1016/s0140-6736(17)33326-3]

Aran, D., Hu, Z. and Butte, A.J., 2017. xCell: digitally portraying the tissue cellular heterogeneity landscape, **18**(1):220. [doi: 10.1186/s13059-017-1349-1]

Becht, E., Giraldo, N.A., Lacroix, L., Buttard, B., Elarouci, N., Petitprez, F., et al., 2016. Estimating the population abundance of tissue-infiltrating immune and stromal cell populations using gene expression, **17**(1):218. [doi: 10.1186/s13059-016-1070-5]

Capitanio, U. and Montorsi, F., 2016. Renal cancer, **387**(10021):894-906. [doi: 10.1016/s0140-6736(15)00046-x]

Chen, B., Khodadoust, M.S., Liu, C.L., Newman, A.M. and Alizadeh, A.A., 2018. Profiling Tumor Infiltrating Immune Cells with CIBERSORT, **1711**(243-259. [doi: 10.1007/978-1-4939-7493-1_12]

Chen, W., Gullett, J.M., Tweedell, R.E. and Kanneganti, T.D., 2023. Innate immune inflammatory cell death: PANoptosis and PANoptosomes in host defense and disease:e2250235. [doi: 10.1002/eji.202250235]

Chen, X., Kang, R., Kroemer, G. and Tang, D., 2021. Organelle-specific regulation of ferroptosis, **28**(10):2843-2856. [doi: 10.1038/s41418-021-00859-z]

Dall'Olio, F.G., Rizzo, A., Mollica, V., Massucci, M., Maggio, I. and Massari, F., 2021. Immortal time bias in the association between toxicity and response for immune checkpoint inhibitors: a meta-analysis, **13**(3):257-270. [doi: 10.2217/imt-2020-0179]

Dutta, S., Ganguly, A., Chatterjee, K., Spada, S. and Mukherjee, S., 2023. Targets of Immune Escape Mechanisms in Cancer: Basis for Development and Evolution of Cancer Immune Checkpoint Inhibitors, **12**(2). [doi: 10.3390/biology12020218]

Ellis, M.J., Gillette, M., Carr, S.A., Paulovich, A.G., Smith, R.D., Rodland, K.K., et al., 2013. Connecting genomic alterations to cancer biology with proteomics: the NCI Clinical Proteomic Tumor Analysis Consortium, **3**(10):1108-12. [doi: 10.1158/2159-8290.Cd-13-0219]

Friedman, J., Hastie, T. and Tibshirani, R., 2010. Regularization Paths for Generalized Linear Models via Coordinate Descent, **33**(1):1-22.

Geeleher, P., Cox, N. and Huang, R.S., 2014. pRRophetic: an R package for prediction of clinical chemotherapeutic response from tumor gene expression levels, **9**(9):e107468. [doi: 10.1371/journal.pone.0107468]

Gurung, P., Anand, P.K., Malireddi, R.K., Vande Walle, L., Van Opdenbosch, N., Dillon, C.P., et al., 2014. FADD and caspase-8 mediate priming and activation of the canonical and noncanonical Nlrp3 inflammasomes, **192**(4):1835-46. [doi: 10.4049/jimmunol.1302839]

Guven, D.C., Sahin, T.K., Erul, E., Rizzo, A., Ricci, A.D., Aksoy, S., et al., 2022. The association between albumin levels and survival in patients treated with immune checkpoint inhibitors: A systematic review and meta-analysis, **9**(1039121. [doi: 10.3389/fmolb.2022.1039121]

Hänzelmann, S., Castelo, R. and Guinney, J., 2013. GSVA: gene set variation analysis for microarray and RNA-seq data, **14**(7. [doi: 10.1186/1471-2105-14-7]

Hassannia, B., Wiernicki, B., Ingold, I., Qu, F., Van Herck, S., Tyurina, Y.Y., et al., 2018. Nano-targeted induction of dual ferroptotic mechanisms eradicates high-risk neuroblastoma, **128**(8):3341-3355. [doi: 10.1172/jci99032]

Hu, W., Yang, Y., Fan, C., Ma, Z., Deng, C., Li, T., et al., 2016. Clinical and pathological significance of N-Myc downstream-regulated gene 2 (NDRG2) in diverse human cancers, **21**(6):675-82. [doi: 10.1007/s10495-016-1244-3]

Jiang, W., Deng, Z., Dai, X. and Zhao, W., 2021. PANoptosis: A New Insight Into Oral Infectious Diseases, **12**(789610. [doi: 10.3389/fimmu.2021.789610]

Karki, R., Sharma, B.R., Lee, E., Banoth, B., Malireddi, R.K.S., Samir, P., et al., 2020. Interferon regulatory factor 1 regulates PANoptosis to prevent colorectal cancer, **5**(12). [doi: 10.1172/jci.insight.136720]

Karki, R., Sharma, B.R., Tuladhar, S., Williams, E.P., Zalduondo, L., Samir, P., et al., 2021. Synergism of TNF-α and IFN-γ Triggers Inflammatory Cell Death, Tissue Damage, and Mortality in SARS-CoV-2 Infection and Cytokine Shock Syndromes, **184**(1):149-168.e17. [doi: 10.1016/j.cell.2020.11.025]

Karki, R., Sundaram, B., Sharma, B.R., Lee, S., Malireddi, R.K.S., Nguyen, L.N., et al., 2021. ADAR1 restricts ZBP1-mediated immune response and PANoptosis to promote tumorigenesis, **37**(3):109858. [doi: 10.1016/j.celrep.2021.109858]

Ketelut-Carneiro, N. and Fitzgerald, K.A., 2022. Apoptosis, Pyroptosis, and Necroptosis-Oh My! The Many Ways a Cell Can Die, **434**(4):167378. [doi: 10.1016/j.jmb.2021.167378]

Kuriakose, T., Man, S.M., Malireddi, R.K., Karki, R., Kesavardhana, S., Place, D.E., et al., 2016. ZBP1/DAI is an innate sensor of influenza virus triggering the NLRP3 inflammasome and programmed cell death pathways, **1**(2). [doi: 10.1126/sciimmunol.aag2045]

Kyrochristos, I.D., Ziogas, D.E. and Roukos, D.H., 2019. Dynamic genome and transcriptional network-based biomarkers and drugs: precision in breast cancer therapy, **39**(3):1205-1227. [doi: 10.1002/med.21549]

Lamkanfi, M., Kanneganti, T.D., Van Damme, P., Vanden Berghe, T., Vanoverberghe, I., Vandekerckhove, J., et al., 2008. Targeted peptidecentric proteomics reveals caspase-7 as a substrate of the caspase-1 inflammasomes, **7**(12):2350-63. [doi: 10.1074/mcp.M800132-MCP200]

Langfelder, P. and Horvath, S., 2008. WGCNA: an R package for weighted correlation network analysis, **9**(559. [doi: 10.1186/1471-2105-9-559]

Lee, S., Karki, R., Wang, Y., Nguyen, L.N., Kalathur, R.C. and Kanneganti, T.D., 2021. AIM2 forms a complex with pyrin and ZBP1 to drive PANoptosis and host defence, **597**(7876):415-419. [doi: 10.1038/s41586-021-03875-8]

Li, A., Cao, C., Gan, Y., Wang, X., Wu, T., Zhang, Q., et al., 2022. ZNF677 suppresses renal cell carcinoma progression through N6-methyladenosine and transcriptional repression of CDKN3, **12**(6):e906. [doi: 10.1002/ctm2.906]

Li, T., Fan, J., Wang, B., Traugh, N., Chen, Q., Liu, J.S., et al., 2017. TIMER: A Web Server for Comprehensive Analysis of Tumor-Infiltrating Immune Cells, **77**(21):e108-e110. [doi: 10.1158/0008-5472.Can-17-0307]

Lin, J.F., Hu, P.S., Wang, Y.Y., Tan, Y.T., Yu, K., Liao, K., et al., 2022. Phosphorylated NFS1 weakens oxaliplatin-based chemosensitivity of colorectal cancer by preventing PANoptosis, **7**(1):54. [doi: 10.1038/s41392-022-00889-0]

Love, M.I., Huber, W. and Anders, S., 2014. Moderated estimation of fold change and dispersion for RNA-seq data with DESeq2, **15**(12):550. [doi: 10.1186/s13059-014-0550-8]

Lukens, J.R., Gurung, P., Vogel, P., Johnson, G.R., Carter, R.A., McGoldrick, D.J., et al., 2014. Dietary modulation of the microbiome affects autoinflammatory disease, **516**(7530):246-9. [doi: 10.1038/nature13788]

Ma, J., Zhou, W., Yuan, Y., Wang, B. and Meng, X., 2023. PSMD12 interacts with CDKN3 and facilitates pancreatic cancer progression, **30**(8):1072-1083. [doi: 10.1038/s41417-023-00609-y]

Malireddi, R.K., Ippagunta, S., Lamkanfi, M. and Kanneganti, T.D., 2010. Cutting edge: proteolytic inactivation of poly(ADP-ribose) polymerase 1 by the Nlrp3 and Nlrc4 inflammasomes, **185**(6):3127-30. [doi: 10.4049/jimmunol.1001512]

Malireddi, R.K.S., Gurung, P., Kesavardhana, S., Samir, P., Burton, A., Mummareddy, H., et al., 2020. Innate immune priming in the absence of TAK1 drives RIPK1 kinase activity-independent pyroptosis, apoptosis, necroptosis, and inflammatory disease, **217**(3). [doi: 10.1084/jem.20191644]

Malireddi, R.K.S., Gurung, P., Mavuluri, J., Dasari, T.K., Klco, J.M., Chi, H., et al., 2018. TAK1 restricts spontaneous NLRP3 activation and cell death to control myeloid proliferation, **215**(4):1023-1034. [doi: 10.1084/jem.20171922]

Mariathasan, S., Turley, S.J., Nickles, D., Castiglioni, A., Yuen, K., Wang, Y., et al., 2018. TGFβ attenuates tumour response to PD-L1 blockade by contributing to exclusion of T cells, **554**(7693):544-548. [doi: 10.1038/nature25501]

Mayakonda, A., Lin, D.C., Assenov, Y., Plass, C. and Koeffler, H.P., 2018. Maftools: efficient and comprehensive analysis of somatic variants in cancer, **28**(11):1747-1756. [doi: 10.1101/gr.239244.118]

Nallar, S.C., Xu, D.Q. and Kalvakolanu, D.V., 2017. Bacteria and genetically modified bacteria as cancer therapeutics: Current

Unedited

advances and challenges, **89**(160-172. [doi: 10.1016/j.cyto.2016.01.002]

Park, H.H., Kim, H.R., Park, S.Y., Hwang, S.M., Hong, S.M., Park, S., et al., 2021. RIPK3 activation induces TRIM28 derepression in cancer cells and enhances the anti-tumor microenvironment, **20**(1):107. [doi: 10.1186/s12943-021-01399-3]

Plattner, C., Finotello, F. and Rieder, D., 2020. Deconvoluting tumor-infiltrating immune cells from RNA-seq data using quanTIseq, **636**(261-285. [doi: 10.1016/bs.mie.2019.05.056]

Ramachandran, M., Vaccaro, A., van de Walle, T., Georganaki, M., Lugano, R., Vemuri, K., et al., 2023. Tailoring vascular phenotype through AAV therapy promotes anti-tumor immunity in glioma, **41**(6):1134-1151 e10. [doi: 10.1016/j.ccell.2023.04.010]

Rini, B.I., Battle, D., Figlin, R.A., George, D.J., Hammers, H., Hutson, T., et al., 2019. The society for immunotherapy of cancer consensus statement on immunotherapy for the treatment of advanced renal cell carcinoma (RCC), **7**(1):354. [doi: 10.1186/s40425-019-0813-8]

Rizzo, A., Mollica, V., Tateo, V., Tassinari, E., Marchetti, A., Rosellini, M., et al., 2023. Hypertransaminasemia in cancer patients receiving immunotherapy and immune-based combinations: the MOUSEION-05 study, **72**(6):1381-1394. [doi: 10.1007/s00262-023-03366-x]

Rodriguez-Vida, A., Hutson, T.E., Bellmunt, J. and Strijbos, M.H., 2017. New treatment options for metastatic renal cell carcinoma, **2**(2):e000185. [doi: 10.1136/esmoopen-2017-000185]

Santoni, M., Buti, S., Myint, Z.W., Maruzzo, M., Iacovelli, R., Pichler, M., et al., 2024. Real-world Outcome of Patients with Advanced Renal Cell Carcinoma and Intermediate- or Poor-risk International Metastatic Renal Cell Carcinoma Database Consortium Criteria Treated by Immune-oncology Combinations: Differential Effectiveness by Risk Group?, **7**(1):102-111. [doi: 10.1016/j.euo.2023.07.003]

Sato, Y., Yoshizato, T., Shiraishi, Y., Maekawa, S., Okuno, Y., Kamura, T., et al., 2013. Integrated molecular analysis of clear-cell renal cell carcinoma, **45**(8):860-7. [doi: 10.1038/ng.2699]

Stelzer, G., Rosen, N., Plaschkes, I., Zimmerman, S., Twik, M., Fishilevich, S., et al., 2016. The GeneCards Suite: From Gene Data Mining to Disease Genome Sequence Analyses, **54**(1.30.1-1.30.33. [doi: 10.1002/cpbi.5]

Stuart, T., Butler, A., Hoffman, P., Hafemeister, C., Papalexi, E., Mauck, W.M., 3rd, et al., 2019. Comprehensive Integration of Single-Cell Data, **177**(7):1888-1902.e21. [doi: 10.1016/j.cell.2019.05.031]

Subramanian, A., Tamayo, P., Mootha, V.K., Mukherjee, S., Ebert, B.L., Gillette, M.A., et al., 2005. Gene set enrichment analysis: a knowledge-based approach for interpreting genome-wide expression profiles, **102**(43):15545-50. [doi: 10.1073/pnas.0506580102]

Sun, W., Li, P., Wang, M., Xu, Y., Shen, D., Zhang, X., et al., 2023. Molecular characterization of PANoptosis-related genes with features of immune dysregulation in systemic lupus erythematosus, **253**(109660. [doi: 10.1016/j.clim.2023.109660]

Sung, H., Ferlay, J., Siegel, R.L., Laversanne, M., Soerjomataram, I., Jemal, A., et al., 2021. Global Cancer Statistics 2020: GLOBOCAN Estimates of Incidence and Mortality Worldwide for 36 Cancers in 185 Countries, **71**(3):209-249. [doi: 10.3322/caac.21660]

Tang, D., Chen, X., Kang, R. and Kroemer, G., 2021. Ferroptosis: molecular mechanisms and health implications, **31**(2):107-125. [doi: 10.1038/s41422-020-00441-1]

Tang, R., Xu, J., Zhang, B., Liu, J., Liang, C., Hua, J., et al., 2020. Ferroptosis, necroptosis, and pyroptosis in anticancer immunity, **13**(1):110. [doi: 10.1186/s13045-020-00946-7]

The-Cancer-Genome-Atlas-Research-Network, 2013. Comprehensive molecular characterization of clear cell renal cell carcinoma, **499**(7456):43-9. [doi: 10.1038/nature12222]

Thomas, P.D., Ebert, D., Muruganujan, A., Mushayahama, T., Albou, L.P. and Mi, H., 2022. PANTHER: Making genome-scale phylogenetics accessible to all, **31**(1):8-22. [doi: 10.1002/pro.4218]

Uhlén, M., Fagerberg, L., Hallström, B.M., Lindskog, C., Oksvold, P., Mardinoglu, A., et al., 2015. Proteomics. Tissue-based map of the human proteome, **347**(6220):1260419. [doi: 10.1126/science.1260419]

Van Allen, E.M., Miao, D., Schilling, B., Shukla, S.A., Blank, C., Zimmer, L., et al., 2015. Genomic correlates of response to CTLA-4 blockade in metastatic melanoma, **350**(6257):207-211. [doi: 10.1126/science.aad0095]

Walton, J., Lawson, K., Prinos, P., Finelli, A., Arrowsmith, C. and Ailles, L., 2023. PBRM1, SETD2 and BAP1 - the trinity of 3p in clear cell renal cell carcinoma, **20**(2):96-115. [doi: 10.1038/s41585-022-00659-1]

Wang, Z., Gerstein, M. and Snyder, M., 2009. RNA-Seq: a revolutionary tool for transcriptomics, **10**(1):57-63. [doi: 10.1038/nrg2484]

Yoshihara, K., Shahmoradgoli, M., Martínez, E., Vegesna, R., Kim, H., Torres-Garcia, W., et al., 2013. Inferring tumour purity and stromal and immune cell admixture from expression data, **4**(2612. [doi: 10.1038/ncomms3612]

Yu, C., Cao, H., He, X., Sun, P., Feng, Y., Chen, L., et al., 2017. Cyclin-dependent kinase inhibitor 3 (CDKN3) plays a critical role in prostate cancer via regulating cell cycle and DNA replication signaling, **96**(1109-1118. [doi: 10.1016/j.biopha.2017.11.112]

Zhang, M., Zhai, W., Miao, J., Cheng, X., Luo, W., Song, W., et al., 2022. Single cell analysis reveals intra-tumour heterogeneity,

Unedited

microenvironment and potential diagnosis markers for clear cell renal cell carcinoma, **12**(5):e713. [doi: 10.1002/ctm2.713]
Zhang, N., Liu, X., Qin, J., Sun, Y., Xiong, H., Lin, B., et al., 2023. LIGHT/TNFSF14 promotes CAR-T cell trafficking and cytotoxicity through reversing immunosuppressive tumor microenvironment, **31**(9):2575-2590. [doi: 10.1016/j.ymthe.2023.06.015]
Zhang, X., Yu, S., Li, X., Wen, X., Liu, S., Zu, R., et al., 2023. Research progress on the interaction between oxidative stress and platelets: Another avenue for cancer?, **191**(106777. [doi: 10.1016/j.phrs.2023.106777]
Zhao, P., Wang, M., Chen, M., Chen, Z., Peng, X., Zhou, F., et al., 2020. Programming cell pyroptosis with biomimetic nanoparticles for solid tumor immunotherapy, **254**(120142. [doi: 10.1016/j.biomaterials.2020.120142]
Zheng, M., Karki, R., Vogel, P. and Kanneganti, T.D., 2020. Caspase-6 Is a Key Regulator of Innate Immunity, Inflammasome Activation, and Host Defense, **181**(3):674-687.e13. [doi: 10.1016/j.cell.2020.03.040]

Supplementary information
Figs. S1-S4; Tables S1 an S2

Table 1 Baseline characteristic of patients in TCGA-KIRC.

Clinical features	Subtype	Patient numbers	Patient percentage (%)
Age	> 65	185	34.5
	≤ 65	352	65.5
Gender	Male	346	64.4
	Female	191	35.6
Grade	G1	14	2.6
	G2	230	42.8
	G3	207	38.5
	G4	78	14.5
	Unknown	8	1.5
Stage	Stage I	269	50.1
	Stage II	57	10.6
	Stage III	125	23.3
	Stage IV	83	15.5
	Unknown	3	0.6
T-stage	T1	275	51.2
	T2	69	12.8
	T3	182	33.9
	T4	11	2.0
N-stage	N0	240	44.7
	N1	17	3.2
	Unknown	280	52.1
M-stage	M0	426	79.3
	M1	79	14.7
	Unknown	32	6.0

Unedited

Table 2 Baseline characteristic of patients in E-MATB-1980.

Clinical features	Subtype	Patient numbers	Patient percentage (%)
Age	> 65	95	39.6
	≤ 65	145	60.4
Gender	Male	184	76.7
	Female	56	23.3
Grade	G1	42	17.5
	G2	141	58.8
	G3	49	20.4
	G4	6	2.5
	Unknown	2	0.8
T-stage	T1	187	77.9
	T2	18	7.5
	T3	33	13.8
	T4	2	0.8
N-stage	N0	238	99.2
	N1	2	0.8
M-stage	M0	215	89.6
	M1	25	10.4

Unedited

Supplementary figure legend

Fig. S1 Identification of the most ccRCC-related gene module in TCGA-KIRC using the WGCNA method. (a) Scale-free network map. (b) Mean connectivity network map. (c) Network heatmap of genes clustered in different modules. (d) Correlation between important ccRCC genes and genes in the blue module. (e) Correlation between important ccRCC genes and genes in the gray module. (f) Correlation between important ccRCC genes and genes in the turquoise module.

Fig. S2 Immunohistochemical analysis examines the specific overexpression of PANI constituent genes TNFSF14, PTHLH, and HMOX1 in ccRCC. (a) Immunohistochemical comparison of TNFSF14 expression in normal renal tissue and ccRCC. (b) Immunohistochemical comparison of PTHLH expression in normal renal tissue and ccRCC. (c) Immunohistochemical comparison of HMOX1 expression in normal renal tissue and ccRCC. (d) Immunohistochemical comparison of HMOX1 expression in ccRCC tissues with different grades and stages.

Fig S3 Variant landscape of High-PANI group and Low-PANI group. (a, g) Variant Classification of High-PANI group (a) and Low-PANI group (g). (b, h) Variant Classification of High-PANI group (b) and Low-PANI group (h). (c, i) SNV Classification of High-PANI group (c) and Low-PANI group (i). (d, j) Variants per sample summary of High-PANI group

(d) and Low-PANI group (j). (e, k) Variant Classification summary of High-PANI group (e) and Low-PANI group (k). (f, l) Variant Classification of High-PANI group (f) and Low-PANI group (l). (m) K-M curve showing the OS difference between H-TMB and L-TMB group. (n) K-M curve showing the OS difference under different PANI and TMB groupings.

Fig S4 The K-M curve shows the OS difference between the high ImmuneScore group and the low ImmuneScore group.

Unedited